ORIENTATION AND ALIGNMENT OF REACTION PRODUCTS

Andrew J. Orr-Ewing[1] *and Richard N. Zare*

Department of Chemistry, Stanford University, Stanford, California 94305

INTRODUCTION

The individual encounters between reagents and the separation of products from the transition state for a reaction, symbolized by

$$A + BC \rightarrow AB + C, \qquad\qquad 1.$$

are intrinsically anisotropic because certain angles of approach of A to BC and of separation of AB from C are preferred, as are certain planes of rotation of the reagent and product molecules. Most of the experimental and theoretical efforts aimed at understanding elementary reactions have been applied to the study of the scalar properties of Reaction 1, such as how the rate of reaction varies with the energies of the reagents or how the energy available after reaction is partitioned among the internal and translational degrees of freedom of the products. To concentrate exclusively on the scalar properties of the reaction is to neglect, however, the vector properties that are key indicators of the anisotropic forces present in the reaction. Vector properties, such as velocities and angular momenta, possess not only magnitudes that can be directly related to translational and rotational energies, but also well-defined directions. Only by understanding the scalar and vector properties together, as well as possible

---

[1] Current address: School of Chemistry, University of Bristol, Bristol BS8 1TS, U.K.

correlations among them, can the fullest picture of the scattering dynamics for Reaction 1 emerge. In this review, we illustrate the importance of understanding the vector properties for Reaction 1 (summarized in Table 1) (1, 2).

The fields of molecular photodissociation, gas-surface scattering, and inelastic and elastic scattering of molecules have benefited from studies of the anisotropy of the collision process, whether that anisotropy is of molecular velocities or of angular momenta. The focus of this review, however, is on reactive collisions. We place particular emphasis on the connection between the product rotational angular momentum, J_{AB}, and the reagent and product relative velocities. We refer in general terms to anisotropic spatial distributions of J_{AB} as angular momentum polarization. To study vector properties of a scattering process, the spherical symmetry (i.e. the equivalence of all directions in space) of a traditional bulb reaction must be broken. Spatial anisotropy in a collision-dynamics experiment can be achieved in a number of ways including photodissociation of molecules using a polarized laser beam, scattering molecules off a surface, or colliding molecules prepared in directional beams.

We discuss how to describe angular momentum polarization in terms of alignment and orientation parameters and review the experimental techniques available for probing the spatial distributions of angular momentum vectors. We also illustrate the importance of theoretical calculations and experimental measurements of angular momentum polarization for bimolecular reactions.

Table 1   Notation for the vector properties of Reaction 1

Vector	Definition
v_A	Velocity of A in the laboratory frame
v_{BC}	Velocity of BC in the laboratory frame
v_{AB}	Velocity of AB in the laboratory frame
v_C	Velocity of C in the laboratory frame
u	Velocity of the center of mass
k	Relative velocity of reagents
k'	Relative velocity of products
u_{BC}	Velocity of BC in the center-of-mass frame
u_A	Velocity of A in the center-of-mass frame
u_{AB}	Velocity of AB in the center-of-mass frame
u_C	Velocity of C in the center-of-mass frame
J_{BC}	Rotational angular momentum of BC
J_{AB}	Rotational angular momentum of AB
L	Orbital angular momentum of the reagents
L'	Orbital angular momentum of the products

A SIMPLE PICTURE OF ORIENTATION AND ALIGNMENT

We describe here the qualitative meaning of orientation and alignment using simple examples and defer formal definitions of orientation and alignment parameters to a later section. Figure 1 shows ensembles of single-headed and double-headed arrows whose directions are aniso-tropically distributed. The single-headed arrows have a net direction toward the top of the page, and we refer to such a directionality as orientation. Because the double-headed arrows point two ways, they have no net directionality. In the figure, however, they point preferentially toward the top and bottom of the page, as compared to the sides of the page, which indicates that all directions in space are not equivalent. Such an ensemble of double-headed arrows is referred to as being aligned or
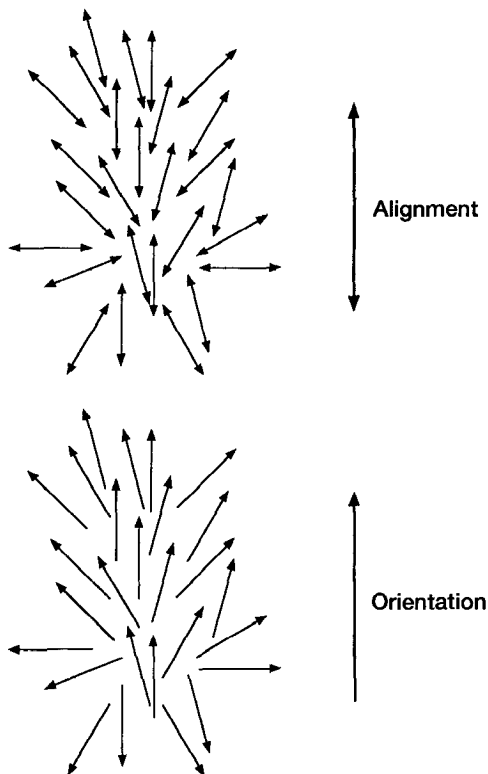
Figure 1   Ensembles of double- and single-headed arrows representing aligned and oriented samples.

possessing alignment. If we think of the arrows as representing rotational angular momentum vectors, $\mathbf{J}$, then an oriented distribution of $\mathbf{J}$ is one in which a preferred direction for $\mathbf{J}$ exists in space. For an aligned sample, however, we can distinguish between $\mathbf{J}$ vectors preferentially pointing either parallel to or perpendicular to some reference direction, but we cannot distinguish parallel from antiparallel.

Most experiments have a symmetry axis, denoted by $\mathbf{Z}$, and we use this axis to describe the anisotropic distribution of $\mathbf{J}$. The symmetry axis might be the direction of a molecular beam or the polarization direction of a linearly polarized laser beam. The distribution of $\mathbf{J}$ has a positive orientation if the angular momentum vectors point preferentially parallel to $\mathbf{Z}$ and a negative orientation if they point preferentially antiparallel to $\mathbf{Z}$ (shown in Figure 2). If the ensemble of $\mathbf{J}$ is aligned, then the alignment is said to be positive if the $\mathbf{J}$ vectors are preferentially parallel or antiparallel
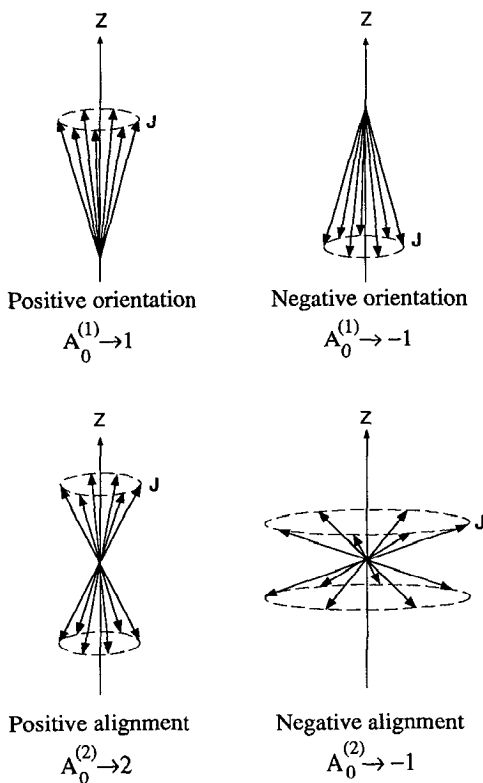

Positive orientation
$A_0^{(1)} \to 1$

Negative orientation
$A_0^{(1)} \to -1$

Positive alignment
$A_0^{(2)} \to 2$

Negative alignment
$A_0^{(2)} \to -1$

Figure 2   Schematic diagram of positively and negatively oriented and aligned distributions.

to Z, and negative if they are preferentially perpendicular to Z (see Figure 2). When the system has cylindrical symmetry about Z and thus the position of J with respect to Z can be defined by only one angle, θ, orientation and alignment are conveniently represented by Legendre polynomial moments. We discuss later what happens when Legendre polynomials are inadequate to describe angular momentum distributions, either because more than one angle is necessary to define the distribution of J about Z (cylindrical symmetry is broken) or because a continuous angular coordinate is inappropriate due to space-quantization effects.

The scalar product of $\hat{J}$ and $\hat{Z}$ (superscript carats denote unit vectors) gives the angle between the two vectors:

$$\hat{J} \cdot \hat{Z} = \cos \theta. \qquad 2.$$

The Legendre polynomials are written as $P_n(\hat{J} \cdot \hat{Z})$, or $P_n(\cos \theta)$, where, for example

$$P_1(\hat{J} \cdot \hat{Z}) = P_1(\cos \theta) = \cos \theta, \qquad 3.$$

and

$$P_2(\hat{J} \cdot \hat{Z}) = P_2(\cos \theta) = \tfrac{1}{2}[3 \cos^2 \theta - 1], \qquad 4.$$

and the Legendre moments, $\langle P_n(\hat{J} \cdot \hat{Z}) \rangle$, are averages of the $P_n(\hat{J} \cdot \hat{Z})$ over the distribution of $\hat{J}$ about $\hat{Z}$. If we write the first- and second-order orientation and alignment parameters as $A_0^{(1)}$ and $A_0^{(2)}$, respectively, the commonly used definitions are

$$A_0^{(1)} = \langle P_1(\hat{J} \cdot \hat{Z}) \rangle = \langle \cos \theta \rangle \qquad 5.$$

and

$$A_0^{(2)} = 2\langle P_2(\hat{J} \cdot \hat{Z}) \rangle = \langle 3 \cos^2 \theta - 1 \rangle. \qquad 6.$$

The suitability of Legendre polynomials is apparent, because for J parallel to Z, $P_1(\hat{J} \cdot \hat{Z}) = 1$ and $P_2(\hat{J} \cdot \hat{Z}) = 1$, whereas for J antiparallel to Z, we still have $P_2(\hat{J} \cdot \hat{Z}) = 1$, but $P_1(\hat{J} \cdot \hat{Z}) = -1$. Thus, the alignment parameter takes the value $A_0^{(2)} = 2$ for parallel and antiparallel arrangements of J and Z, but the orientation parameter, $A_0^{(1)}$, changes sign from $+1$ to -1. For J perpendicular to Z, $A_0^{(1)} = 0$, but the alignment parameter becomes negative: $A_0^{(2)} = -1$. The values of the alignment and orientation parameters discussed above are limiting cases that represent the maximum possible alignment and orientation. In general, these parameters take values of smaller magnitude, which indicates a distribution that tends toward one of the above limits. If all alignment and orientation parameters are zero, the J distribution is isotropic about Z. We also encounter other

alignment parameters, in particular $A_0^{(4)}$, which is commonly called the hexadecapolar alignment since it is related to $P_4(\hat{\mathbf{J}} \cdot \hat{\mathbf{Z}})$ [$A_0^{(2)}$ is called the quadrupolar alignment]. The hexadecapolar alignment is described in a later section, but it is qualitatively similar to the quadrupolar alignment. Note that whereas an oriented sample may also be aligned, aligned samples commonly have no orientation.

ANGULAR MOMENTUM POLARIZATION IN CHEMICAL REACTIONS

The term dynamical stereochemistry is widely used (3–6) to describe the study of the angular anisotropy of the forces that control a chemical reaction and the consequences of these anisotropic forces on the spatial polarization of reagent and product velocities and angular momenta. Aspects of dynamical stereochemistry have been reviewed by Bernstein et al (3), Simons (4), Houston (7), and Levine (6), and have been the subject of three special issues of journals (8–10). We review here the experimental measurement and theoretical calculation of one aspect of dynamical stereochemistry, product rotational alignment and orientation. The goal of dynamical stereochemistry is to understand the chemical shapes of molecules as opposed to their physical shapes, which are obtained from spectroscopy. The notion of chemical shape describes how a molecule's reactivity depends on its separation and angle of approach from another reagent [i.e. the angular dependence of the potential energy surface (PES) for reaction]. The chemical shape differs depending on the species with which a molecule reacts. Herschbach (11) has likened the forces controlling a reaction (i.e. the PES) to a polarizing lens that induces a preferred directionality to product velocities and angular momenta. The product velocity and angular momentum vectors therefore provide us with a probe of the anisotropy of the PES.

Experimental Measurements of Orientation and Alignment of Reaction Products

Herschbach and coworkers (11–17) undertook pioneering experiments to determine alignment moments for the products of various reactions using crossed beams and an analyzer consisting of an inhomogeneous electric field region. The analyzer deflected the differently aligned molecular rotations to varying degrees. Analysis of the deflection profiles revealed the preferred second Legendre moment, and in a few cases the fourth Legendre moment, of the angular momentum distribution about the relative velocity for the reagents. The experiments were insensitive to different internal states of the product because of the use of a universal surface

ionization detector, and the scattering angles of the products in the center-of-mass frame were not resolved. In several reactions, such scattering-angle resolution is not possible because the mass combinations of reagents and products ($H + HL \rightarrow HH + L$, with H denoting a heavy atom and L denoting a light atom) result in a scattering of products along the center-of-mass velocity direction.

The systems studied by Herschbach and coworkers (11–17) include the reactions of K with HBr and Br_2, and Cs with HBr, HI, CH_3I, CCl_4, and Br_2; the experimenters detected the products KX or CsX (X = Cl, Br, or I). The products were found to be strongly rotationally aligned, with J_{CsX} or J_{KX} perpendicular to the reagent relative velocity for reaction with HBr and HI; the products were substantially aligned for the reaction of Cs with CH_3I; and they were unpolarized for reaction with Br_2 and CCl_4. The results of this work are summarized in Table 2. Later work by Hsu & Herschbach (13), in which nonadiabatic changes in the quantization axis within the electric-deflection analyzer were eliminated, found moderate alignment for the Cs and $K + Br_2$ reaction products. For the reaction of Cs with CH_3I, Hsu, McClelland & Herschbach (14) measured the correlation between the k,k' plane and the J_{CsI} vector, thereby breaking the azimuthal symmetry of the scattering about k.

The large negative value of $A_0^{(2)}$ for the reaction of the metal atoms with HX can be understood in terms of kinematic constraints (18). In Reaction 1, the conservation of angular momentum requires that

$$L + J_{BC} = L' + J_{AB} \qquad\qquad 7.$$

(see Table 1 for the definition of all vectors). For $H + HL$ systems, typically $|L| \gg |J_{BC}|$ because the large reduced mass of the reagents ensures a large orbital angular momentum, whereas BC has a large rotational constant and is often cooled in a beam expansion. For the products, comparison of the orbital and rotational angular momentum magnitudes suggests that $|L'| \ll |J_{AB}|$ because the heavy AB diatomic molecule has a small rotational constant, and the small reduced mass of the products results in a small product orbital angular momentum. The approximate conservation equation,

$$L \approx J_{AB}, \qquad\qquad 8.$$

therefore constrains J_{AB} to be perpendicular to k because k is necessarily perpendicular to L. Such kinematic constraints have been examined in greater detail by Noda & Zare (19) in their constant product recoil (CPR) model and by Simons and coworkers (20), who calculated the translational energy dependence of the product rotational alignment for $H + HL \rightarrow HH + L$ mass combination systems based on their constant-product,

orbital-angular-momentum (CPOAM) model. The latter model allows for the contribution to the total angular momentum balance from product orbital angular momentum, and it permits estimates of the division of the angular momentum disposal between J_{AB} and L' and of the exit-channel impact parameter. Simons and coworkers (20) find that, in many cases, the kinematic limit is approached only at high collision energies.

Zare and coworkers (21) were the first to use optical transitions to probe the alignment of reaction products. The origin of the sensitivity of absorption and emission processes to angular momentum alignment and orientation is discussed later. Jonah et al (21) employed visible chemi-luminescence with a polarization analyzer to obtain the second-order

Table 2 Alignment parameters for the products of bimolecular reactions

Reaction	Experimental method	Collision energy (meV)	$A_0^{(2)}$	References
$Cs + HI$	Electric deflection	100	-0.88 ± 0.08	15
$Cs + HBr$	Electric deflection	90	-0.76 ± 0.08	15
$K + HBr$	Electric deflection	80	-0.84 ± 0.12	15
$K + Br_2$	Electric deflection	Thermal beam	-0.24	13
$Cs + Br_2$	Electric deflection	Thermal beam	-0.20	13
$Cs + CF_3I$	Electric deflection	Thermal beam	-0.24	13
$Cs + CH_3I$	Electric deflection	Thermal beam	-0.24	13
$Cs + CCl_4$	Electric deflection	Thermal beam	-0.12	13
$Cs + SF_4$	Electric deflection	Thermal beam	-0.04	13
$Cs + SF_6$	Electric deflection	Thermal beam	-0.08	13
$Xe^* + Br_2$	Chemiluminescence	60	-0.28 ± 0.06	29
$Xe^* + CCl_4$	Chemiluminescence	60	-0.02 ± 0.02	29
$Xe^* + ICl$	Chemiluminescence	60	-0.02 ± 0.04	29
$Xe^* + CH_3I$	Chemiluminescence	60	-0.46 ± 0.06	29
$Xe^* + CF_3I$	Chemiluminescence	60	-0.14 ± 0.14	29
$Xe^* + BrCN$	Chemiluminescence	60	0.00 ± 0.04	27
$Ca^* + HCl$	Chemiluminescence	70	-0.88 ± 0.04	22, 35
		45	-0.82 ± 0.04	
$Ba + NO_2$	Chemiluminescence	70	-0.10 ± 0.04	21
$Ba + N_2O$	Chemiluminescence	70	<0	21
$Sr + NO_2$	Chemiluminescence	70	0	21
$Sr + N_2O$	Chemiluminescence	70	<0	21
$Ca^* + F_2$	LIF	—	-0.06 ± 0.04	34
$Ca^* + HF$	LIF	—	-0.73 ± 0.02	34
$Ba + N_2O$	Chemiluminescence	160	-0.2 to -0.50	172[a]
$Xe^* + CH_3I$	Chemiluminescence	60	-0.39	33[b]
		200	-0.57	
$Xe^* + CH_2I_2$	Chemiluminescence	200	-0.5	33[b]
$Xe^* + CH_2Br_2$	Chemiluminescence	200	-0.4	33[b]

Table 2—(*continued*)

Reaction	Experimental method	Collision energy (meV)	$A_0^{(2)}$	References
Xe* + CHBr$_3$	Chemiluminescence	200	−0.25	33[b]
Xe* + CBr$_4$	Chemluminescence	200	−0.24	33[b]
Xe* + CHCl$_3$	Chemiluminescence	200	−0.1	33[b]
Xe* + CCl$_4$	Chemiluminescence	60	−0.03	33[b]
		200	−0.06	
Kr* + CBr$_4$	Chemiluminescence	200	−0.2	33[b]
Sr + CH$_3$Br	Chemiluminescence	—	−0.34 ± 0.04	37
Sr + C$_2$H$_5$Br	Chemiluminescence	—	−0.24 ± 0.04	37
Sr + C$_3$H$_7$Br	Chemiluminescence	—	−0.14 ± 0.04	37
O(^{3}P) + CS	LIF	—[c]	0	39, 41[d]
O(^{1}D) + N$_2$O	LIF	—[c]	0 to −1	43[e]
O(^{1}D) + CH$_4$	LIF	—[c]	−0.12 ± 0.56	45[f]
O(^{1}D) + H$_2$O	LIF	—[c]	0	47
H + O$_2$	LIF	—[c]	−1	48[g]
H + O$_2$	LIF	—[c]	0 OH(A″) <0 OH(A′)	49[h]

[a] Alignment measured for three different orientations of the reagent N$_2$O.

[b] Further alignment parameters are presented for different collision energies in this reference. Note that the definition of alignment used in this reference is the negative of the more widespread definition used in this chapter. For collision energies for the Xe* + CCl$_4$ reaction lower than 50 meV, the alignment changes sign.

[c] For hot-atom reactions under bulb conditions we do not cite collision energies, as the uncertainties in this energy due to the internal degrees of freedom of X from AX photolysis and the thermal motion of the photolysis precursor and target gas are large (38).

[d] Alignment measured for many different CO(v, J) states.

[e] Alignment measured for many NO(v, J) states.

[f] Alignment value for OH($v' = 4, N' = 8$).

[g] Alignment parameters deduced from their experimental data.

[h] The OH alignment differs for the two Λ-doublet components of the ground $^2\Pi$ state (see text for details).

alignment moments for the reactions of Ba and Sr with N$_2$O and NO$_2$. They demonstrated how to relate the degree of polarization of the chemiluminescence emitted on either a parallel or a perpendicular transition to the alignment of the electronically excited products using a classical treatment. For the reactions of Ba with NO$_2$ and Ba and Sr with N$_2$O, Jonah et al (21) found the emission to be weakly polarized but detected no polarization for the Sr + NO$_2$ reaction. Prisant et al (22) subsequently studied reactions of Ca(^{1}D) with HCl and found the CaCl(B$^2\Sigma^+$) to be strongly aligned as a result of kinematic constraints. They attributed deviation from the limiting alignment of −1 to the H atom carrying away some orbital angular momentum. In studies of the Ca(^{1}S$_0$) + F$_2$ reaction, Prisant et al (23) resolved a vibrational-state dependence to the CaF(B$^2\Sigma^+$)

chemiluminescence polarization and, hence, a vibrational-state dependence to the product rotational alignment.

Simons and coworkers have performed crossed-beam and beam-gas studies of reactions of electronically excited rare-gas atoms with halogen-containing molecules. Rettner & Simons (24, 25) examined the reactions of $Xe(^3P_{0,2})$ with Br_2 and CCl_4 in a crossed-beam apparatus with polarization resolution of the XeX* chemiluminescence. The xenon beam was accelerated using a magnetically levitated rotor. This combination permitted measurements of the product alignment as a function of the collision energy from thermal energies up to 1.25 eV. Hennessy et al (26–29) studied the reactions of $Xe(^3P_{0,2})$ with CH_3Br, CH_3I, ICl, CF_3I, CCl_4, and BrCN and the reaction of $Kr(^3P_{0,2})$ with Br_2 in the same way, and they used simple models to assess the relative importance of kinematic and dynamic effects in the reactive scattering. Johnson et al (30) studied the reactions of $Xe(^3P_{0,2})$ formed in a rotor-accelerated beam with thermal gases of HCl; this work was extended to include the reactions of $Xe(^3P_{0,2})$ with Cl_2 and I_2. Johnson et al (31) observed a dependence of the product alignment on the collision energy; the polarization of J_{XeX} perpendicular to k became more pronounced as the collision energy increased. Martin and coworkers (32, 33) also used polarized-chemiluminescence detection to probe the velocity dependence of the rotational alignment of the excimer species formed in the reaction of $Xe(^3P_{0,2})$ with a series of halogenated methanes, CH_3I, CH_2I_2, CH_2Br_2, $CHBr_3$, CBr_4, $CHCl_3$, and CCl_4. They found that the XeX* rotational alignment increased in magnitude as collision energy and halogen mass increased and the number of halogen atoms per molecule decreased. Engelke & Meiwes-Broer (34) examined the Ca*+HF and $Ca+F_2$ reactions using crossed beams and LIF detection; they found a much-reduced polarization in the second reaction as compared with the kinematically constrained first reaction. González-Ureña and coworkers (35, 36) have studied the reaction of $Ca(^1D_2)$ with HCl under beam-gas conditions at a collision energy lower than that used by Prisant et al (22) and fitted the alignment parameters at the two collision energies examined with the CPOAM model. Recent work by Li et al (37) on the reactions of Sr with RBr (R = CH_3, C_2H_5, n-C_3H_7, and i-C_3H_7) showed an increasingly negative quadrupolar alignment as the size of R decreases.

Despite the possibility of dispersing the chemiluminescence and resolving transitions to individual vibrational and rotational states, the problems of low signal levels have restricted quantum-state-resolved alignment measurements studied under beam-gas or crossed-beam conditions to one example to date, the reaction of $Ca(^1S_0)+F_2$, in which the alignment for different vibrational transitions was determined (23). Laser-probing schemes [laser-induced fluorescence (LIF) and resonance-enhanced multi-

photon ionization (REMPI)] are more sensitive than chemiluminescence detection and have allowed rotational- and vibrational-state-resolved measurements to be made of angular momentum polarization for the products of bimolecular reactions. This progress is also a consequence of the development of techniques for measuring product rotational alignment under bulb conditions, in which photodissociation is used to generate what have been called translationally aligned or velocity-aligned reagents (this terminology is not to be confused with the usual use of alignment to describe angular-momentum vector or molecular axis distributions). The use of translationally aligned reagents results in greater signal levels than crossed-beam and beam-gas experiments but at the expense of a greater uncertainty in the collision energy (38).

Hancock and coworkers (39, 40) used NO_2 photolysis to produce $O(^3P)$. They studied the reaction of the oxygen atoms with CS, which yields vibrationally excited $CO(X^1\Sigma^+)$. The CO product was detected using polarized LIF. They found the CO unaligned with respect to $\mathbf{k}$ to within the precision of the measurements for many rotational and vibrational states. The reaction has no kinematic constraints, and a comparison with quasiclassical trajectory (QCT) calculations (41) suggested three possible causes of the zero alignment. The first was that reaction at large impact parameters, observed in the QCT calculation, could be associated with a redirection of the relative velocity at short range. The second was that a memory of $\mathbf{k}$ was lost because of snarled trajectories that passed through short-lived complexes with a shorter lifetime than the complex's rotational period. The final possibility was that the calculated and experimentally observed angular scattering was only weakly forward and backward peaking, so strong polarization of $\mathbf{J}_{CO}$ about $\mathbf{k}'$ (which was observed) is washed out when looking at the $\mathbf{J}_{CO}$ distribution about $\mathbf{k}$. Brouard et al have also conducted photoinitiated bulb experiments; they used photolysis of N_2O to make translationally aligned $O(^1D)$ and studied the reactions with N_2O (42–44) and CH_4 (45). In the former case, they found that the NO product had a negative alignment parameter. Ben-Nun et al (46) proposed a peripheral reaction mechanism to account for the observation that $\mathbf{J}_{NO}$ points preferentially perpendicular to the relative velocity, with $O(^1D)$ stripping a nitrogen atom and the remaining NO fragment acting as a spectator. In the reaction of $O(^1D)$ with CH_4, the OH formed in $v' = 4$, $N' = 8$, showed a weak negative alignment of its angular momentum about $\mathbf{k}$ but a stronger alignment of the angular momentum perpendicular to the product OH velocity.

King and coworkers (47) applied the technique of velocity-aligned reagent experiments in a bulb to the reaction of $O(^1D)$ with H_2O and found the OH product to have zero alignment within experimental uncertainties.

They attributed this finding to the fact that the reaction exothermicity constitutes 80% of the available energy, meaning energy release in the reaction can overcome the initial kinematics and reorient fragment rotations. Kleinermanns & Linnebach (48) studied the $H + O_2$ reaction with LIF detection of OH but did not invert their polarization data to obtain an alignment parameter. A later analysis of this data by Brouard (M Brouard, personal communication) suggested an alignment of approximately -1. Subsequent work by Hall and coworkers (49) that used 193-nm photolysis of H_2S to form translationally hot and aligned H atoms showed no polarization dependence to the intensity of the OH LIF recorded for Q-branch transitions. Hall and coworkers (49) concluded that the OH formed in the A″ Λ-doublet state, which is probed by the Q-branch LIF transition, is not aligned. An involved analysis that accounted for the contributions to the OH LIF Doppler lineshape from the reaction differential cross section and the distribution of J_{OH} vectors suggested that the OH formed in the A′ Λ-doublet component, probed by P and R branches, is highly aligned with J_{OH} perpendicular to the OH product velocity in the center-of-mass frame; hence, J_{OH} is perpendicular to the reagent relative velocity as the OH is forward scattered. These conclusions have been explained in terms of a planar reaction transition state forming OH that is rotationally aligned and predominantly in the A′ symmetry Λ-doublet component. Collisions with the O-atom product in the exit valley of the PES can result in either Λ-doublet-conserving scattering, which is known to conserve M (50, 51), or Λ-doublet-changing scattering, which is known to be strongly depolarizing. The techniques available for studying dynamical stereochemistry in bulb experiments are discussed in a later section. Table 2 summarizes much of the alignment data available for bimolecular reactions.

In addition to the alignment of the rotational angular momentum of a molecule formed in a chemical reaction, the internal angular momenta of the electrons can also be aligned, and this orbital alignment is a valuable indicator of the nature of chemical reaction dynamics (43, 44, 47, 52–59). A thorough discussion of orbital alignment, however, is beyond the scope of this review.

Theoretical Calculations of Product Orientation and Alignment

Only limited theoretical calculations, using either quasiclassical trajectory methods or quantum-scattering or wavepacket-propagation techniques, have been made of angular momentum polarization, perhaps because of a shortage of experimental data with which to make comparisons. Hijazi & Polanyi (60, 61) used QCT methods on two potential energy surfaces, one attractive and one repulsive, to investigate the effects of different

mass combinations of reagents and products on the distribution of angles between J_{AB} and k. The degree of angular momentum polarization becomes less marked as the mass combinations change from $H + HL$ to $L + LL$ to $L + HH$, i.e. as reagent orbital angular momentum contributes less to the total angular momentum. On the repulsive surface, they found that for the $L + LL$ mass combination, for which there are no strong kinematic constraints, the strongest rotational polarization (J_{AB} perpendicular to k) corresponded to backward scattered products. This behavior was not observed on the attractive PES.

Early converged three-dimensional, quantum-mechanical scattering calculations by Schatz & Kuppermann (62) on the $H + H_2$ atom-exchange reaction resolved the cross sections into different product M states and revealed a propensity for the $H + H_2(J, M = 0) \rightarrow H_2(J', M' = 0) + H$ reaction channel to dominate the reactive scattering for low values of J. This calculation has yet to be verified experimentally. Blais & Truhlar (63) studied the $H + Br_2$ reaction using QCT methods and evaluated the moments of the HBr rotational angular momentum distribution as a function of the scattering angle. The calculated differential cross section was backward peaked, but the rotational alignment was calculated to be strongest for sideways-scattered products. For the reaction of Mg with HF, Alvariño & Laganà (64, 65) determined the degree of alignment of the product MgF from QCT calculations. The MgF can be formed by two classes of trajectories: direct scattering and trajectories that pass through a well on the PES. The calculations show a substantially decreased degree of rotational alignment for the MgF formed via the complex mechanism. Hancock and coworkers (41) performed QCT calculations on the reaction of $O(^3P)$ with CS to compare the CO alignment from the calculations with that observed experimentally. An empirical London-Eyring-Polanyi-Sato (LEPS) potential energy surface optimized using vibrational and rotational quantum-state population distributions of the CO reproduced the experimentally measured near-zero product rotational alignment. The calculated negative value of the correlation between k' and J' also agreed with the experimental data.

Extensive work by Alexander and coworkers (66–69) and Kouri and coworkers (70–72) established a theoretical framework for the propensity for M-state conserving and changing collisions in inelastic scattering. In particular, Alexander and coworkers (66, 67) demonstrated that for inelastic scattering dominated by long-range parts of the potential (the weak-coupling or l-dominant regime, sampled by large impact parameter collisions), product alignment is favored; whereas for scattering dominated by the short-range, repulsive part of the potential (the strong-coupling or potential-dominant regime, sampled by small impact parameter colli-

sions), the degree of product alignment is expected to be small or non-existant.

Simple models for reactive scattering, in particular the direct interaction with product repulsion (DIPR) model, have been used to calculate product rotational alignment and orientation (73). The DIPR model assumes a strong repulsive energy release in the reagent BC followed by capture of B and A. This simplified model thus permits an evaluation of the contribution of such repulsive energy release to product angular momentum distributions without the added effects of complicated potential energy surfaces. McClelland & Herschbach (74) and Prisant et al (73) applied the DIPR model to the analysis of their experimental results. The former authors found that the DIPR model predicted that J_{AB} would lie preferentially perpendicular to the plane of k and k'. Herschbach and co-workers also considered a statistical treatment of vector correlations (75–77), which has made an information-theory analysis possible (78).

DEFINITIONS OF ORIENTATION AND ALIGNMENT PARAMETERS

Orientation and alignment parameters provide a convenient method of describing the distribution of angular momentum vectors about some reference (quantization) axis, which might be the relative velocity of the reagents in, for example, a crossed-beam experiment, or the polarization vector of the laser used in a photodissociation experiment. When the reference axis is an axis of cylindrical symmetry (also referred to as azimuthal or axial symmetry), the orientation and alignment parameters can be related to the fractional number of vectors J that point in a particular direction with respect to the symmetry axis, i.e. in a quantum-mechanical picture, to the populations of the M states. When cylindrical symmetry is broken, the orientation and alignment parameters contain information not only on M-state populations, but also on the phase relationships between the $|JM\rangle$ eigenstates in the ensemble, and these phase relationships are called coherences. In a cylindrically symmetric system, the coherences of the ensemble vanish, and the ensemble is an incoherent superposition of the $|JM\rangle$ states. Cylindrical symmetry is common in collision dynamics experiments; for example, in a crossed-beam experiment, the reagent relative velocity vector is an axis of cylindrical symmetry, as is the beam axis in a beam-gas experiment and the electric vector of a linearly polarized laser in a photodissociation experiment or in a reaction-dynamics experiment using hot atoms from a photolysis source. Thus, for such experiments, only the orientation and alignment parameters that describe

M-state populations are typically measured, but if the cylindrical symmetry is broken, coherence terms must also be taken into account.

In the limit of large angular momentum (the high-J limit), $\mathbf{J}$ may be treated as being continuously distributed about the symmetry axis (the projection of $\mathbf{J}$ on the symmetry axis is described by the quantum number M, but for large angular momenta, the interval between projection angles that correspond to allowed values of M becomes small). In this limit we can therefore treat the spatial distribution of $\mathbf{J}$ classically. For low values of the angular momentum, only discrete values of the projection angle of $\mathbf{J}$ onto the symmetry axis are permitted, and the distribution of $\mathbf{J}$ is more conveniently described using the populations and coherences of the M quantum states. An isotropic distribution of $\mathbf{J}$ corresponds to equal populations of all the M states with no phase relationship between them, whereas certain M states or (M, M') coherences or both are favored for an anisotropic distribution.

Classical Description of Rotational Angular Momentum Distributions

In the classical limit, the location of a vector $\mathbf{J}$ about a symmetry axis $\mathbf{Z}$ is parametrized by the (continuously distributed) polar coordinates θ and ϕ. For the simplest case of cylindrical symmetry of $\mathbf{J}$ about $\mathbf{Z}$, the distribution has no dependence on the angle ϕ. The distribution of $\mathbf{J}$, denoted here by $N(\hat{\mathbf{J}}, \hat{\mathbf{Z}})$, with the carats, as before, indicating unit vectors, can be written as an expansion in Legendre polynomials (79):

$$N(\hat{\mathbf{J}}, \hat{\mathbf{Z}}) = \frac{1}{4\pi} \sum_n a_n P_n (\cos \theta), \qquad 9.$$

where the index, n, runs over zero and all positive integers. The coefficients of the expansion give the moments of the distribution:

$$a_n = (2n+1)\langle P_n(\cos\theta)\rangle = (2n+1) \int_0^{2\pi} d\phi \int_0^\pi \sin\theta \, d\theta \, N(\hat{\mathbf{J}}, \hat{\mathbf{Z}}) P_n (\cos\theta),$$

$$10.$$

and for cylindrical symmetry, the alignment and orientation parameters are defined in terms of the Legendre moments. The chosen normalizations are conventional; they give convenient limits on the alignment and orientation parameters. A second convention is to describe odd moments of the distribution as orientation parameters and even moments as alignment parameters. We use the notation throughout that an alignment or orientation parameter of order k and component q ($q = 0$ only for cylindrical symmetry; otherwise, $-k \leqslant q \leqslant k$) is denoted by $A_q^{(k)}(J)$ regardless of

whether k is odd or even, rather than the notation of $O_q^{(k)}(J)$ for orientation parameters and $A_q^{(k)}(J)$ for alignment parameters as is used sometimes in the literature (80–82). We define (80–82)

$$A_0^{(0)}(J) = 1,$$
11.

$$A_0^{(1)}(J) = \langle P_1(\hat{\mathbf{J}} \cdot \hat{\mathbf{Z}}) \rangle = \langle P_1(\cos\theta) \rangle \quad \text{range} -1 \text{ to } 1,$$
12.

$$A_0^{(2)}(J) = 2\langle P_2(\hat{\mathbf{J}} \cdot \hat{\mathbf{Z}}) \rangle = 2\langle P_2(\cos\theta) \rangle \quad \text{range} -1 \text{ to } 2,$$
13.

$$A_0^{(3)}(J) = \langle P_3(\hat{\mathbf{J}} \cdot \hat{\mathbf{Z}}) \rangle = \langle P_3(\cos\theta) \rangle \quad \text{range} -1 \text{ to } 1,$$
14.

and

$$A_0^{(4)}(J) = \langle P_4(\hat{\mathbf{J}} \cdot \hat{\mathbf{Z}}) \rangle = \langle P_4(\cos\theta) \rangle \quad \text{range} -\tfrac{3}{7} \text{ to } 1,$$
15.

which restricts the ranges of the alignment parameters as indicated. These ranges are valid in the high-J limit. Product-orientation moments have been measured in photodissociation (83, 84) and gas-surface scattering experiments (85), but surprisingly, to the best of our knowledge, have not been probed in reactive-scattering experiments. To date, the $A_0^{(3)}(J)$ moment has been probed only in experimental studies of gas-surface scattering (85).

The angular distribution of $\mathbf{J}$ can be expanded in terms of the multipolar moments as

$$N(J, \theta) = \frac{1}{4\pi} \{ A_0^{(0)}(J) + 3A_0^{(1)}(J)P_1(\cos\theta) + \tfrac{5}{2}A_0^{(2)}(J)P_2(\cos\theta)$$

$$+ 7A_0^{(3)}(J)P_3(\cos\theta) + 9A_0^{(4)}(J)P_4(\cos\theta) + \ldots \}.$$
16.

The $A_0^{(0)}(J)$ moment describes the (monopole) population of the rotational state with angular momentum $\mathbf{J}$. For an isotropic distribution of $\mathbf{J}$, it is the only nonzero term in Equation 16. The $A_0^{(1)}(J)$ moment represents the contribution to the anisotropy of a dipolar distribution of $\mathbf{J}$ about $\mathbf{Z}$; $A_0^{(2)}(J)$ represents the quadrupolar contribution to the anisotropy; $A_0^{(3)}(J)$ represents the octopolar contribution; and $A_0^{(4)}(J)$ represents the hexadecapolar contribution. For the odd moments, forward ($\theta = 0°$) and backward directions ($\theta = 180°$) are distinguishable, as discussed earlier, whereas these directions cannot be distinguished for even moments.

In the limit that $\mathbf{J}$ is perpendicular to the molecular axis, $\mathbf{r}$, we can describe the spatial distribution of the molecular axes in a similar way to Equation 16. If we denote the angle between the $\mathbf{r}$ and the cylindrical-symmetry axis by χ, then a specialization of the spherical harmonic

addition theorem (82) [termed the aximuthally averaged addition (AAA) theorem (77)] gives

$$\langle P_n(\cos\chi)\rangle = P_n\left(\cos\frac{\pi}{2}\right)\langle P_n(\cos\theta)\rangle. \qquad 17.$$

Consequently, the Legendre expansion for the molecular axis alignment (the orientation terms vanish) is (86)

$$N(J,\chi) = \frac{1}{4\pi}\{1 - \tfrac{5}{4}A_0^{(2)}(J)P_2(\cos\chi) + \tfrac{27}{8}A_0^{(4)}(J)P_4(\cos\chi) - \ldots\}. \qquad 18.$$

The alignment of **r** is less than the alignment of **J** because **J** is space fixed, whereas **r** is rotating in the space-fixed frame.

If the distribution of **J** about **Z** is not azimuthally symmetric, i.e. if the cylindrical symmetry is broken, then the angular distribution can be expanded in terms of spherical harmonics (82), and alignment parameters can be defined in an analogous fashion to the moments above. Note that in this instance, alignment parameters with $q \neq 0$ can arise, and these describe the distribution of the projection of **J** onto the XY plane.

Quantum-Mechanical Description of Angular Momentum Distributions

The definition of orientation and alignment parameters for low values of the magnitude of **J** makes use of spherical tensors (82) and density matrices (87). The density-matrix formulation is convenient to describe the coherence terms that arise when cylindrical symmetry is broken and a phase relationship exists between $|JM\rangle$ and $|JM'\rangle$ states. The multipole moments of the angular momentum spherical-tensor operator, $J_q^{(k)}$, are given by (82, 87)

$$\langle J_q^{(k)}\rangle = \langle(J|J_q^{(k)}|J)\rangle = \sum_{M,M'} \rho_{M'M}\langle JM|J_q^{(k)}|JM'\rangle, \qquad 19.$$

where the $\rho_{M'M}$ are density-matrix elements describing the polarized ensemble. It is often advantageous to write the density matrix, ρ, in terms of state multipoles because of the straightforward transformation properties of the state multipoles under rotation. We summarize here the use of state multipoles and state-multipole moments and their connection to the angular momentum spherical-tensor moments defined above. We denote the state-multipole moments by $\rho_q^{(k)}(J)$, although Blum (87) and others have used the notation $\langle T(J)_{kq}^\dagger\rangle$. Following Blum (87), we decompose the density matrix as

$$\rho = \sum_{k,q} \rho_q^{(k)}(J) T_q^{(k)}. \tag{20}$$

The $T_q^{(k)}$ are called state multipoles (88) and are spherical-tensor operators of rank k and component q. Blum (87) gives the relationships between $\rho_{M'M}$ and $\rho_q^{(k)}(J)$:

$$\rho_q^{(k)}(J) = \sum_{M,M'} (-1)^{J-M'} (2k+1)^{1/2} \begin{pmatrix} J & k & J \\ -M & -q & M' \end{pmatrix} \rho_{M'M}, \tag{21}$$

$$\rho_{M'M} = \sum_{k,q} (-1)^{J-M'} (2k+1)^{1/2} \begin{pmatrix} J & k & J \\ -M & -q & M' \end{pmatrix} \rho_q^{(k)}(J). \tag{22}$$

A connection is made to the expectation values of the angular momentum spherical-tensor operators via the Wigner-Eckart theorem (82):

$$\rho_{-q}^{(k)}(J) = (-1)^q \langle J_q^{(k)} \rangle \frac{\sqrt{2k+1}}{(J \| J^{(k)} \| J)}, \tag{23}$$

where the reduced matrix elements in the denominator are well known (82), and we have made use of a standard result for the reduced matrix elements of the state multipoles.

From Equations 22 and 23, we can relate the density-matrix elements to the moments of $J_q^{(k)}$ by

$$\rho_{M'M} = \sum_{k,q} (-1)^{J+q-M'} \frac{(2k+1)}{(J \| J^{(k)} \| J)} \begin{pmatrix} J & k & J \\ -M & q & M' \end{pmatrix} \langle J_q^{(k)} \rangle, \tag{24}$$

and, thus, the diagonal elements of the density matrix, which contain information about the populations of the magnetic sublevels, are

$$\rho_{MM} = \sum_{k} (-1)^{J-M} \frac{(2k+1)}{(J \| J^{(k)} \| J)} \begin{pmatrix} J & k & J \\ -M & 0 & M \end{pmatrix} \langle J_0^{(k)} \rangle. \tag{25}$$

(The $3j$ symbol in Equation 24 vanishes for $M = M'$ unless $q = 0$.)

Orientation and alignment parameters are traditionally defined in terms of the spherical-tensor angular momentum operator $J_q^{(k)}$ (82, 89–91) by

$$A_q^{(k)}(J) = \frac{c(k)}{\langle JM | \mathbf{J}^2 | JM \rangle^{k/2}} Re \langle J_q^{(k)} \rangle. \tag{26}$$

Because of its rotational transformation properties, we find it advantageous to define an alternative parameter, denoted by $\mathscr{A}_q^{(k)}(J)$, that retains the complex part of the angular momentum spherical-tensor moments:

$$\mathcal{A}_q^{(k)}(J) = \frac{c(k)}{\langle JM|\mathbf{J}^2|JM\rangle^{k/2}}\langle J_q^{(k)}\rangle. \qquad 27.$$

In Equations 26 and 27, $c(k)$ is a normalization constant chosen such that the moments with $q = 0$ coincide with the definitions given in the preceding section in the high-J limit:

$$c(0) = 1, \quad c(1) = 1, \quad c(2) = \sqrt{6}, \quad c(3) = \sqrt{5/2},$$

$$\text{and} \quad c(4) = \sqrt{35/8}. \qquad 28.$$

The definition employed in Equation 26 is well established and consistently used in the literature, and we therefore retain the symbol $A_{\pm q}^{(k)}(J)$ to accompany this definition when reviewing previous studies of angular momentum polarization. From Equation 26, it follows that

$$A_{-q}^{(k)}(J) = (-1)^q A_q^{(k)}(J). \qquad 29.$$

The definitions of Equations 26 and 27 can be inserted into Equations 24 and 25 to express the diagonal and off-diagonal density-matrix elements in terms of orientation and alignment parameters.

$$\rho_{M'M} = \sum_{k,q}(-1)^{J+q-M'}\frac{(2k+1)[J(J+1)]^{k/2}}{c(k)(J\|J^{(k)}\|J)}\begin{pmatrix} J & k & J \\ -M & q & M' \end{pmatrix}\mathcal{A}_q^{(k)}(J). \qquad 30.$$

We can write the diagonal elements of the density matrix as fractional populations of the $|JM\rangle$ states, $p(J, M)$, and can express the population over M states for a given J in terms of the alignment moments with $q = 0$:

$$\rho_{MM} = p(J, M) = (-1)^{J-M}\sum_{k}\frac{(2k+1)[J(J+1)]^{k/2}}{c(k)(J\|J^{(k)}\|J)}$$

$$\times\begin{pmatrix} J & k & J \\ -M & 0 & M \end{pmatrix}\mathcal{A}_0^{(k)}(J). \qquad 31.$$

In Equation 31 we could use $A_0^{(k)}(J)$ parameters in place of the $\mathcal{A}_0^{(k)}(J)$ because for $q = 0$, all alignment parameters are real.

The reciprocal relationships are obtained directly from Equation 19. For nonzero values of the component q,

$$\mathcal{A}_q^{(k)}(J) = \frac{c(k)}{\langle JM|\mathbf{J}^2|JM\rangle^{k/2}}\sum_{M,M'}\rho_{M'M}\langle JM|J_q^{(k)}|JM'\rangle \qquad 32.$$

and

$$A_q^{(k)}(J) = Re[\mathscr{A}_q^{(k)}(J)] = \frac{c(k)}{\langle JM|\mathbf{J}^2|JM\rangle^{k/2}} Re\left[\sum_{M,M'} \rho_{M'M}\langle JM|J_q^{(k)}|JM'\rangle\right],$$

33.

where the off-diagonal density-matrix elements, $\rho_{M'M}$, contain coherence information.

A molecular ensemble with $J = 0$ cannot show alignment or orientation, whereas for $J = 1/2$, an ensemble may possess a first-order orientation moment. For $J = 1$, the highest possible moments that can exist are $A_{\pm q}^{(2)}(J)$ or $\mathscr{A}_{\pm q}^{(2)}(J)$, whereas for $J = 2$, moments as high as $A_{\pm q}^{(4)}(J)$ or $\mathscr{A}_{\pm q}^{(4)}(J)$ can arise.

The concept of coherences is illustrated in a highly simplified way in Figure 3, in which distributions of angular momentum vectors, $\mathbf{J}$, about a quantization axis, $\mathbf{Z}$, are shown for a single value of the projection quantum number, M. The angular-momentum spherical-tensor operators with $q = 0$ are constructed from the operators $\mathbf{J}$ and J_Z (82), and thus the parameters $A_0^{(k)}(J)$ describe the distribution of projections of the angular momentum vectors of a molecular ensemble onto the $\mathbf{Z}$ axis. The angular-momentum spherical-tensor operators with nonzero components, $J_q^{(k)}$, contain contributions from the operators J_X and J_Y, and thus, the alignment and orientation parameters, $A_q^{(k)}(J)$, with $q \neq 0$, contain information about XY-plane projection of the rotational angular momentum distribution. As illustrated schematically in Figure 3, if the distribution of $\mathbf{J}$ is cylindrically symmetric about $\mathbf{Z}$, no net projection of the angular-momentum distribution exists in the XY-plane, and the $A_q^{(k)}(J)$ vanish for $q \neq 0$ (the figure illustrates an oriented ensemble, although a similar figure could be obtained for an aligned sample by using double-headed arrows). The $\mathbf{J}$ distribution, however, has a net projection along $\mathbf{Z}$, and the $A_0^{(k)}(J)$ parameters are nonzero. If no cylindrical symmetry exists about $\mathbf{Z}$, or if a frame rotation introduces a new quantization axis, $\mathbf{Z}'$, with associated axes X' and Y', nonzero projection of the $\mathbf{J}$ distribution may result in the XY or $X'Y'$ planes, respectively (Figure 3); thus, the orientation and alignment parameters with $q \neq 0$ can take nonzero values. These conditions for a new projection onto the XY plane require a nonrandom distribution of the azimuthal angles about the quantization axis ($\mathbf{Z}$ or $\mathbf{Z}'$), i.e. some coherence must exist among the $\mathbf{J}$ vectors of the molecular ensemble.

In certain applications, the real tensor operators, $J_{q\pm}^{(k)}$, and their associated orientation and alignment moments, $A_{q\pm}^{\{k\}}(J)$ and $\mathscr{A}_{q\pm}^{\{k\}}(J)$, are required. These parameters are connected by the definition (89)–(91):

$$\mathscr{A}_{q\pm}^{\{k\}}(J) = A_{q\pm}^{\{k\}}(J) = \frac{c(k)}{\langle JM|\mathbf{J}^2|JM\rangle^{k/2}} \langle J_{q\pm}^{\{k\}}\rangle,$$

34.
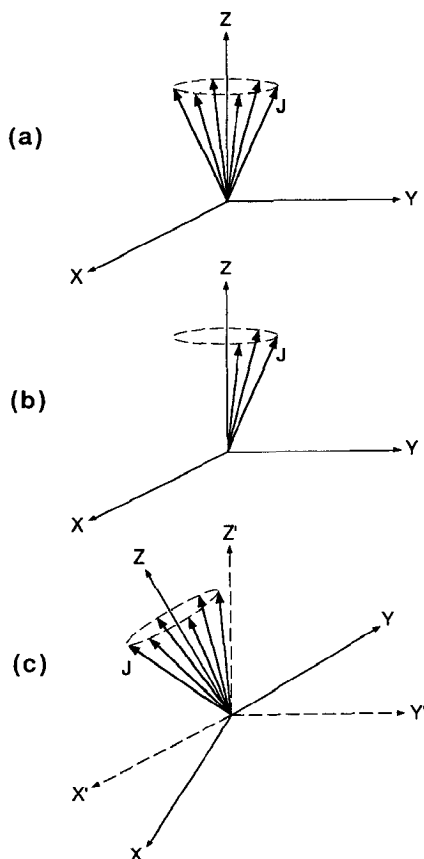
Figure 3 A simple representation of coherence effects: (*a*) a cylindrically symmetric distribution of **J** exhibits no coherences in the X, Y, Z frame; (*b*) a noncylindrically symmetric distribution of **J** exhibits coherences in the X, Y, Z frame; and (*c*) a frame rotation from X, Y, Z to X', Y', Z' breaks the cylindrical symmetry of the **J** distribution, giving rise to coherences in the X', Y', Z' frame.

where we introduce the Hertel & Stoll (92) definitions of real spherical tensor operators:

$$J_{q+}^{\{k\}} = \frac{1}{\sqrt{2}}\{(-1)^q J_q^{(k)} + J_{-q}^{(k)}\} \quad \text{for} \quad 0 < q \leqslant k, \qquad 35.$$

$$J_{q-}^{\{k\}} = \frac{1}{\sqrt{2}i}\{(-1)^q J_q^{(k)} - J_{-q}^{(k)}\} \quad \text{for} \quad 0 < q \leqslant k, \qquad 36.$$

$$J_{0+}^{\{k\}} = J_0^{(k)},$$

37.

and

$$J_{0-}^{\{k\}} = 0.$$

38.

Following Kummel et al (89–91), we distinguish the two types of alignment parameter, $A_{\pm q}^{(k)}(J)$ and $A_{q\pm}^{\{k\}}(J)$, by the use of parentheses, ( ), or braces, { }, around k, as shown in Equations 32 and 36, and use the same notation for $\mathscr{A}_{\pm q}^{(k)}(J)$ and $\mathscr{A}_{q\pm}^{\{k\}}(J)$. Algebraic forms of $J_{q\pm}^{\{k\}}$ and $A_{q\pm}^{\{k\}}(J)$ are tabulated elsewhere (91).

The choice of definition of alignment parameters in terms of the real part of the angular momentum spherical-tensor operator (Equation 26) poses difficulties in relating the $A_{\pm q}^{(k)}(J)$ parameters to the $A_{q\pm}^{\{k\}}(J)$ parameters because the $A_{q\pm}^{\{k\}}(J)$ parameters do not comply with the Hertel & Stoll construction. We note that a measurement of $A_{q-}^{\{k\}}(J)$ gives information on the imaginary parts of the moments of the spherical-tensor operator, and this information cannot be obtained from the other orientation and alignment parameters. One advantage of our modified definition of Equation 27 is that the $\mathscr{A}_{\pm q}^{(k)}(J)$ parameters can be combined to form real orientation and alignment moments using Hertel & Stoll's method, i.e. we can define $\mathscr{A}_{q\pm}^{\{k\}}(J)$ in the same way as $J_{q\pm}^{\{k\}}$ in Equations 35–38.

The Connection Between Orientation and Alignment Parameters and State-Multipole Moments

Within the literature on rotational angular momentum anisotropy, use is made of an alignment-parameter description of angular momentum distributions (39, 40, 43, 80, 81, 89–91, 93–96) and of state multipoles (79, 97–103). Thus, the relationship between the state-multipole moments and alignment parameters that follows from Equations 26 and 27 is

$$\mathscr{A}_q^{(k)}(J) = \frac{(-1)^q c(k)}{\langle JM|\mathbf{J}^2|JM\rangle^{k/2}} \frac{(J\|J^{(k)}\|J)}{\sqrt{2k+1}} \rho_{-q}^{(k)}(J),$$

39.

and

$$A_q^{(k)}(J) = \frac{(-1)^q c(k)}{\langle JM|\mathbf{J}^2|JM\rangle^{k/2}} \frac{(J\|J^{(k)}\|J)}{\sqrt{2k+1}} Re\{\rho_{-q}^{(k)}(J)\}.$$

40.

Equation 39 shows that the $\mathscr{A}_{\pm q}^{(k)}(J)$ parameters are simply state-multipole moments that have been renormalized to fit the familiar high-J limits for orientation and alignment parameters with $q = 0$.

The definitions used in this section allow us to describe angular momen-

tum distributions, populations of $|JM\rangle$ states, and phase relationships between the $|JM\rangle$ states in terms of orientation and alignment parameters. In the following sections, we show how the orientation and alignment parameters can be measured in collision-dynamics experiments.

MEASURING ORIENTATION AND ALIGNMENT PARAMETERS VIA OPTICAL PROBES

In principle, the absorption or emission of photons by a molecule provides a means of determining the plane of rotation of that molecule in space because the transition-dipole moment for the spectroscopic transition is constrained by symmetry requirements to only certain locations with respect to the molecular framework or the rotational angular momentum vector (104, 105). Thus, an anisotropic distribution of angular-momentum vectors in space must be associated with an anisotropic distribution of transition-dipole moments, and this latter anisotropy will influence the degree of absorption or emission of different light polarizations for different solid angles. In a simplistic picture, the quadrupolar (double-headed arrow) nature of linearly polarized light makes this polarization sensitive to alignment moments, whereas the dipolar nature of circularly polarized light results in this type of light being sensitive to orientation moments. Elliptically polarized light can be used to probe both orientation and alignment moments. These qualitative deductions are confirmed by a rigorous treatment of the interaction of polarized light with oriented and aligned ensembles of molecules.

The relationships between the molecular axis, rotational angular momentum, and transition-dipole moment for a diatomic molecule in the high-J limit are shown in Figure 4. For a parallel transition, μ lies along the molecular axis for the P and R branches (there is no Q branch), whereas for a perpendicular transition, μ is perpendicular to the molecular axis. In this case, μ can lie either parallel to $\mathbf{J}$ (for a Q-branch transition) or perpendicular to $\mathbf{J}$ (for an R- or a P-branch transition).

Theoretical treatments have been developed within quantum-mechanical formalisms and the classical, high-J limit to relate the polarization dependence of chemiluminescence, laser-induced fluorescence, and resonance-enhanced multiphoton ionization probes to the spatial anisotropy of $\mathbf{J}$. Taatjes & Stolte (106) recently calculated the polarization dependence of electric-quadrupole/magnetic-dipole transitions, but we concentrate on electric-dipole-allowed processes because of their much wider applicability. Hefter & Bergmann (107) have reviewed the application of spectroscopic techniques to detect atoms and molecules subsequent to scattering processes.
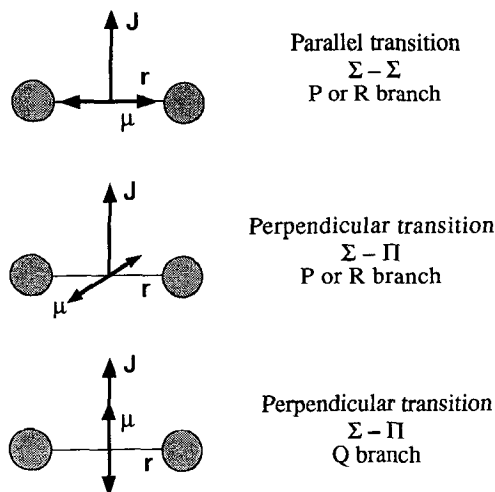
Figure 4 The connection between the rotational angular momentum, **J**, the transition-dipole moment, μ, and the molecular axis, **r**, for a diatomic molecule in the high-J limit. The figure shows the relationship between **J**, μ, and **r** for Q- and P, R-branches for parallel and perpendicular transitions.

The theoretical treatments demonstrate that for one-photon-detection methods, such as the use of chemiluminescence detection or absorption spectroscopy, the highest moments that can be measured using circularly polarized light are the first orientation moments, $A^{(1)}_{\pm q}(J)$. If linearly polarized light is used in the one-photon process, the highest moments that can be probed are the first alignment moments, $A^{(2)}_{\pm q}(J)$. Detecting moments higher than these using optical methods requires the use of probe techniques involving more than one photon, such as $(1+1)$ LIF, two-photon absorption, and $(2+1)$ REMPI; for two-photon processes with circularly and linearly polarized light, the moments $A^{(3)}_{\pm q}(J)$ and $A^{(4)}_{\pm q}(J)$, respectively, can be investigated.

If the experimental system has cylindrical symmetry, the orientation and alignment parameters describing the angular momentum polarization generally can be extracted straightforwardly because only those parameters with $q = 0$ can be nonzero. When the cylindrical symmetry is broken, however, orientation and alignment parameters with $q \neq 0$ can take nonzero values, and for many experimental configurations, these parameters cannot be measured independently. Rather than being sensitive to the orientation and alignment parameters, the experiments can be sensitive to apparent moments that are linear combinations of the true orientation and alignment parameters (89–91). Additional complications arise from

hyperfine depolarization of alignment and saturation of optical transitions, and we discuss these situations below.

We stress that to obtain populations of rotational quantum states, even for isotropic samples with no M-state propensities, an accurate treatment requires consideration of the following discussion. The reason is that the absorption of photons creates an anisotropy in the excited molecular states, and, thus, subsequent photon absorption or emission is from an aligned or oriented sample.

Classical Treatment of Spectral Intensities

In the classical treatment we write the distribution of angular momentum vectors as an expansion in spherical harmonics for noncylindrically symmetric systems or an expansion in Legendre polynomials for azimuthally symmetric systems, as given in Equation 16. The coefficients of the expansion are related in the latter case to Legendre moments and orientation and alignment parameters as described in an earlier section. Case et al (79) gave classical expressions for the $(1+1)$ LIF signal intensity for detection of an aligned sample, and Docker (96) has tabulated the expressions for one-photon absorption or chemiluminescence, $(1+1)$ LIF, and two-photon spectroscopic intensities in terms of alignment parameters for the commonly used experimental geometries.

In beam-gas chemiluminescence detection experiments, two polarization ratios are commonly used and can be related to alignment parameters. If we denote the beam axis by $\mathbf{Z}$, then the degree of polarization, P, is defined by (22)

$$P = \frac{I_\| - I_\perp}{I_\| + I_\perp}, \qquad\qquad 41.$$

where the chemiluminescence intensity polarized parallel to the beam axis is $I_\|$ and the intensity polarized perpendicular to the beam axis is $I_\perp$. The degree of polarization can be related to the second Legendre moment of the distribution of $\mathbf{J}$ about $\mathbf{Z}$ via

$$\langle P_2(\hat{\mathbf{J}} \cdot \hat{\mathbf{Z}}) \rangle = \frac{4P}{P-3} \quad \text{for a P or R line (μ perpendicular to $\mathbf{J}$)} \qquad 42.$$

or

$$\langle P_2(\hat{\mathbf{J}} \cdot \hat{\mathbf{Z}}) \rangle = \frac{2P}{3-P} \quad \text{for a Q line (μ parallel to $\mathbf{J}$).} \qquad 43.$$

The polarization index, or polarization anisotropy, R, is defined by (30, 82)

$$R = \frac{I_{\parallel} - I_{\perp}}{I_{\parallel} + 2I_{\perp}} \qquad 44.$$

and can be related to $\langle P_2(\hat{\mathbf{J}} \cdot \hat{\mathbf{Z}}) \rangle$ via

$$\langle P_2(\hat{\mathbf{J}} \cdot \hat{\mathbf{Z}}) \rangle = -2R$$

$$\text{for a P or R branch transition } (\boldsymbol{\mu} \text{ perpendicular to } \mathbf{J}) \qquad 45.$$

or

$$\langle P_2(\hat{\mathbf{J}} \cdot \hat{\mathbf{Z}}) \rangle = R \quad \text{for a Q branch transition } (\boldsymbol{\mu} \text{ parallel to } \mathbf{J}). \qquad 46.$$

The relationship between $\langle P_2(\hat{\mathbf{J}} \cdot \hat{\mathbf{Z}}) \rangle$ and the alignment of $\mathbf{J}$ with respect to the relative velocity vector in beam-gas experiments is discussed in a subsequent section.

Quantum-Mechanical Description of Spectral Intensities

Several authors have addressed the use of polarized light, particularly linearly polarized light, for the extraction of alignment and orientation parameters via LIF or REMPI. Case et al (79) used a density-matrix procedure to describe $(1+1)$ LIF, while Greene & Zare (81, 93) employed a spherical tensor approach similar to that of Fano & Macek (80). Kummel et al (90) and Waldeck et al (108) extended this work to include elliptically polarized light. McCaffery and coworkers (97, 98, 101, 102) also considered the use of linearly and circularly polarized one-photon absorption, emission, and LIF to obtain moments of the $\mathbf{J}$ distribution. Jacobs & Zare (94) discussed the use of $(1+1)$ REMPI with linearly polarized light and an azimuthally symmetric system. Two-photon absorption has been analyzed by Bain & McCaffery (98–100, 103), Chen & Yeung (109), Dubs et al (110), Docker (96, 111), and Kummel et al (89, 91). We restrict our review of the use of polarized light to determine alignment and orientation moments to the spherical tensor methodology of Greene & Zare (81, 93), Kummel et al (89–91), and Jacobs & Zare (94), and we discuss the use of linearly circularly, and elliptically polarized light. There are close similarities among the analyses of data obtained from the different spectroscopic processes, and we emphasize here the common connections.

The intensity of a probe process, whether 1-photon absorption or chemiluminescence, $(1+1)$ LIF, $(1+1)$ REMPI, or $(2+1)$ REMPI with linearly, elliptically, or circularly polarized photons, can be expressed in a simple form in terms of alignment parameters (81, 89–91, 93, 108):

$$I = C(\det)n(J_i)\sum_{k,q}[P_{q+}^{\{k\}}(J_i,\Lambda_i,J_e,\Lambda_e,J_f,\Lambda_f;\Omega)A_{q+}^{\{k\}}(J_i)$$

$$+ P_{q-}^{\{k\}}(J_i,\Lambda_i,J_e,\Lambda_e,J_f,\Lambda_f;\Omega)A_{q-}^{\{k\}}(J_i)]. \quad 47.$$

$C(\det)$ is a constant that accounts for such experimental factors as the detector sensitivity, the probe-laser intensity, and the number density of product molecules in the probe region, and $n(J_i)$ is the population of the products in state J_i. J_e and J_f label the excited and final states of the spectroscopic process as shown in Figure 5 for $(1+1)$ LIF and $(2+1)$ REMPI. For two-photon absorption schemes such as $(2+1)$ REMPI, there is no dependence on the state $|J_e,\Lambda_e)$ in Equation 47. The index k is the multipole moment of the combined spectroscopic process [e.g. $k = 0, 2,$ 4 for $(1+1)$ LIF with linearly polarized light]. The symmetrized alignment parameters, $A_{q\pm}^{\{k\}}(J_i)$, are related to the standard alignment parameters and were defined in an earlier section. For many standard excitation and detection geometries, Equation 47 can be reduced to the simpler form:

$$I = C(\det)n(J_i)\sum_{k,q}P_q^{(k)}(J_i,\Lambda_i,J_e,\Lambda_e,J_f,\Lambda_f;\Omega)A_q^{(k)}(J_i). \quad 48.$$

The alignment parameters are referenced to the symmetry axis of the experiment about which the polarization of the probe is varied. The

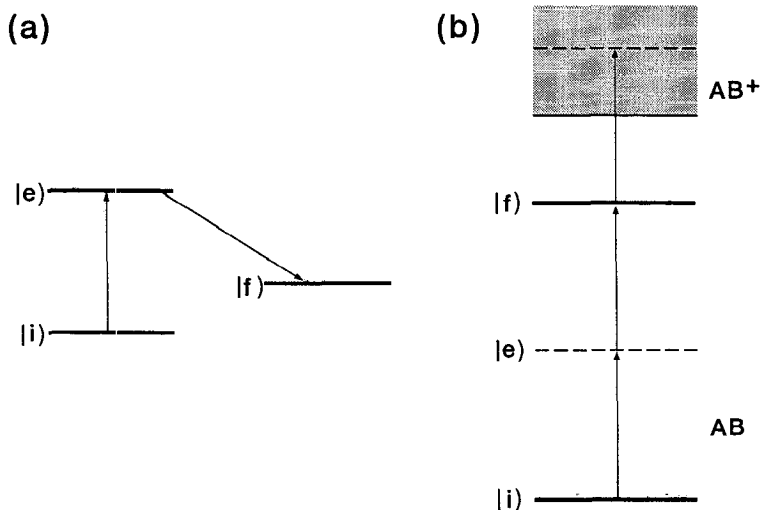*Figure 5* (*a*) The laser-induced fluorescence scheme. Laser excitation from $|J_i)$ to $|J_e)$ is followed by fluorescence from $|J_e)$ to $|J_f)$. (*b*) Energy-level scheme for a $(2+1)$ REMPI process. Two-photon absorption from an initial state $|J_i)$ to a final state of the neutral species, $|J_f)$, proceeds via virtual states labeled by $|J_e)$, and is followed by an ionization step.

$P_q^{(k)}(J_i, \Lambda_i, J_e, \Lambda_e, J_f, \Lambda_f; \Omega)$ and $P_{q\pm}^{\{k\}}(J_i, \Lambda_i, J_e, \Lambda_e, J_f, \Lambda_f; \Omega)$ terms have been called line-strength moments and contain all the information pertaining to the spectral transition, such as its line strength and symmetry and the experimental geometry (denoted here simply by the set of angles Ω). Calculation of the $P_q^{(k)}(J_i, \Lambda_i, J_e, \Lambda_e, J_f, \Lambda_f; \Omega)$ and $P_{q\pm}^{\{k\}}(J_i, \Lambda_i, J_e, \Lambda_e, J_f, \Lambda_f; \Omega)$ values is involved, but Greene & Zare (81, 93) and Kummel et al (89–91) have derived analytic forms for most cases of interest. The forms of the line-strength moments differ for the different types of spectroscopic probe. Their calculation requires the evaluation of Wigner $6j$ and $9j$ symbols, but computer programs are available for this task (82).

The principle behind the experimental determination of the alignment parameters is that the line-strength moments change their values for different spectroscopic transitions (e.g. for O, P, Q, R, and S branches) and for different polarization angles, laser-propagation directions, fluorescence polarizations, and fluorescence-detection directions (we refer to these directions as the experimental geometry). The variation of the $P_q^{(k)}(J_i, \Lambda_i, J_e, \Lambda_e, J_f, \Lambda_f; \Omega)$ or $P_{q\pm}^{\{k\}}(J_i, \Lambda_i, J_e, \Lambda_e, J_f, \Lambda_f; \Omega)$ terms can, however, be calculated using formulas summarized in references (81, 89–91, 93). Thus, by measuring the signal intensities, whether by chemiluminescence, LIF, or REMPI, for different experimental geometries and/or spectral transitions, the alignment and orientation parameters can be deduced. The more geometries used, the more overdetermined the alignment parameters are and, thus, the more accurately they can be deduced (with more meaningful estimates of their associated errors). For a system completely described by two alignment parameters, say $A_0^{(0)}(J_i)$ and $A_0^{(2)}(J_i)$, two experimental geometries or detection via two different spectral branches are sufficient to determine the full M-state distribution.

Widespread use has been made of the above analysis in collisional dynamics experiments. For example, as discussed earlier, investigators using $(1+1)$ LIF with linearly polarized light have measured alignment parameters for the NO product of the reaction of $O(^1D)$ with N_2O (42, 43), the OH products of the reactions of $O(^1D)$ with H_2O (47) and CH_4 (45), and the CO product of the reaction of $O(^3P)$ with CS (39–41). Numerous studies have examined the alignment of photodissociation products, particularly OH, NO, and CN (7, 112), and LIF detection was used to study the alignment of CuF desorbed from a Cu (111) surface following association of surface-bound F atoms with Cu atoms (113).

Studies of N_2 scattering from an Ag (111) surface have used $(2+2)$ REMPI with linearly polarized light to measure the N_2 alignment moments (114, 115), and elliptically polarized light to measure the orientation moments (85). The same detection scheme has been used to study collisional relaxation of aligned N_2 prepared by stimulated Raman pumping

(116). The N_2 scattering experiments have now been extended to include a $(2+1)$ REMPI detection scheme (117), and we are currently using $(2+1)$ REMPI of HCl via the $F^1\Delta$ state in our laboratory to probe the alignment of this product of the $Cl(^2P_{3/2})+CH_4(v_3 = 1, J)$ reaction. The photolysis of CD_3I has been studied using $(2+1)$ REMPI detection of CD_3 (118–120) and also of $I(^2P_{3/2})$ and $I(^2P_{1/2})$ (120). Houston and coworkers (121) investigated the 248-nm photodissociation of O_3 using $(2+1)$ REMPI detection of $O_2(a^1\Delta_g)$ via a $^1\Pi_g$ Rydberg state combined with ion imaging.

The technique developed by Jacobs & Zare (94) for analysing $(1+1)$ REMPI spectra to obtain orientation and alignment data differs substantially in form from the methods of Greene & Zare (93) and Kummel et al (89–91). The differences arise because of the concerns of saturation, either in the first absorption step or in the ionization step, and the possibility of competition between ionization and stimulated emission to the ground state. Such concerns do not arise in $(2+1)$ REMPI because the transition to the ground state is at twice the laser frequency, and because at the high laser powers used to drive the two-photon absorption step, ionization of the excited state is typically saturated. $(1+1)$ REMPI has not yet been used to measure rotational alignment or orientation for the products of a bimolecular reaction, but Jacobs et al (95, 122–125) demonstrated that NO inelastically scattered from a Pt (111) surface has its rotational angular momentum preferentially aligned parallel to the surface (cartwheel-type motion). NO desorbed from the surface, however, has **J** preferentially perpendicular to the surface (helicopter-type motion).

Hyperfine and Spin Depolarization

The degree of rotational alignment or orientation of a molecule can be altered by coupling the rotational angular momentum, **J**, to external fields or to the nuclear or electronic spins of the molecule (80, 82, 87, 126–128). In the study of bimolecular reactions, such depolarization effects can significantly alter the alignment or orientation of prepared reagents because, in general, reaction will not occur immediately upon preparation of the reagents. Likewise, coupling to external fields or intramolecular spin angular momenta will affect the nascent polarization of **J** of reaction products during the time delay between reaction and detection. We concentrate here on the effect of intramolecular couplings by first considering the effect of one nuclear spin, denoted by **I**, such as in OH or CH, and then describing the effect of two nuclear spins encountered in molecules such as HF and HCl. We make the assumptions that (a) at the instant of formation of molecules in an aligned or oriented ensemble, whether by optical pumping or reaction, the rotational angular momentum is uncoupled from the spin angular momenta, but the different momenta

then couple to give a resultant **F**, and (*b*) the nuclear or electronic spins are unpolarized at the instant of formation. We concentrate on nuclear-spin hyperfine-depolarization effects but also note that such considerations apply to molecules with nonzero electronic spin **S**. In such cases, we can describe the depolarization of the total angular momentum excluding spin **N**, which is caused by coupling to **S**, to give a resultant total angular momentum **J** (129).

We can picture the depolarization of **J** in terms of the vector model of angular momenta; **J** and **I** couple to give **F**, and then **J** precesses about **F** so that the prepared direction of **J** in space is lost to some degree. For values of **J** substantially larger than the magnitude of **I**, **J** and **F** will be nearly parallel, and the hyperfine depolarization will be small. For magnitudes of **J** close to or smaller than those of **I**, hyperfine depolarization can severely reduce the degree of orientation or alignment. Derivations of the extent of depolarization for a molecule with a single nuclear spin are given in terms of a state-multipole treatment by Blum (87), and in terms of a spherical-tensor-operator treatment by Zare (82). If the rotational angular momentum distribution at the instant of formation of the aligned or oriented ensemble (time, $t = 0$) is described by multipole moments of the rotational angular momentum spherical-tensor operator, $\langle J_q^{(k)} \rangle_{t=0}$, then at some later time t, the multipole moments are given by

$$\langle J_q^{(k)} \rangle_t = G^{(k)}(t) \langle J_q^{(k)} \rangle_{t=0}, \qquad\qquad 49.$$

where $G^{(k)}(t)$ is a time-dependent depolarization coefficient:

$$G^{(k)}(t) = \sum_{F,F'} \frac{(2F'+1)(2F+1)}{(2I+1)} \begin{Bmatrix} F' & F & k \\ J & J & I \end{Bmatrix}^2 \cos\left[(E_{F'} - E_F)t/\hbar\right]. \qquad 50.$$

In this equation, the E_F are the eigenvalues of the hyperfine Hamiltonian, i.e. they are the energy levels arising from the coupling of the rotational and nuclear spin angular momenta. They can be calculated from hyperfine coupling constants. Note that the interaction between **J** and **I** does not mix multipole moments of **J**, but it does result in a decrease in their value over time. The function $G^{(k)}(t)$ is oscillatory and seldom returns to its original value of unity. The time-averaged value of $G^{(k)}(t)$ is useful for measurements made on a timescale longer than the oscillation period of $G^{(k)}(t)$ and is given by

$$\langle G^{(k)} \rangle = \frac{1}{(2I+1)} \sum_F (2F+1)^2 \begin{Bmatrix} F & F & k \\ J & J & I \end{Bmatrix}^2. \qquad\qquad 51.$$

Fano & Macek (80) discussed the effect of the coupling of two spins,

and Altkorn et al (127, 130) derived an expression for the depolarization coefficient for depolarization by two nuclear spins, I_1 and I_2:

$$G^{(k)}(t) = \frac{1}{(2I_1+1)(2I_2+1)} \sum_{\substack{\alpha,\alpha' \\ F,F'}} (2F'+1)(2F+1)$$

$$\times \left| \sum_{F_i,F_i'} (-1)^{F_i+F_i'} [(2F_i+1)(2F_i'+1)]^{1/2} \right.$$

$$\left. \times c_{\alpha F_i}^{(F)} c_{\alpha' F_i'}^{(F)*} \begin{Bmatrix} F_i' & F' & I_2 \\ F & F_i & k \end{Bmatrix} \begin{Bmatrix} J & F_i' & I_1 \\ F_i & J & k \end{Bmatrix} \right|^2 \cos\left[(E_{\alpha F} - E_{\alpha' F'})t/\hbar\right], \quad 52.$$

which has a long-time averaged form:

$$\langle G^{(k)} \rangle = \frac{1}{(2I_1+1)(2I_2+1)} \sum_{\alpha,F} (2F+1)^2 \left| \sum_{F_i,F_i'} (-1)^{F_i+F_i'} [(2F_i+1)(2F_i'+1)]^{1/2} \right.$$

$$\left. \times c_{\alpha F_i}^{(F)} c_{\alpha F_i'}^{(F)*} \begin{Bmatrix} F_i' & F & I_2 \\ F & F_i & k \end{Bmatrix} \begin{Bmatrix} J & F_i' & I_1 \\ F_i & J & k \end{Bmatrix} \right|^2. \quad 53.$$

In a hierarchical-coupling scheme, $\mathbf{J}$ and $\mathbf{I}_1$ couple together to give $\mathbf{F}_i$, and $\mathbf{F}_i$ subsequently couples to $\mathbf{I}_2$ to give the total angular momentum $\mathbf{F}$. In the limit of a hierarchical-coupling scheme, F_i is a good quantum number. When such a hierarchical-coupling scheme is not applicable, α replaces F_i as an intermediate quantum number. Assigning particular values to α is not necessary because they serve only as labels to differentiate between states. The states that diagonalize the hyperfine Hamiltonian are labeled by F and α in this instance. Orr-Ewing et al (131) calculated the time-dependence of the depolarization coefficients for HCl for which $\mathbf{I}_{Cl} = 3/2$ and $\mathbf{I}_H = 1/2$. The calculation correctly predicted the observed time dependence of the REMPI intensity ratio for two laser polarizations.

Suppose that the product molecules are formed aligned by a reaction initiated at time $t = 0$ and are probed at a later time t. Then three regimes of hyperfine depolarization can be distinguished. If we ascribe a characteristic timescale to the hyperfine depolarization, denoted τ, defined by

$$\frac{1}{\tau} = |E_{\alpha F} - E_{\alpha' F'}|/\hbar, \qquad 54.$$

the regimes are

1. $t \ll \tau$: The hyperfine depolarization can be neglected.
2. $t \gg \tau$: The hyperfine depolarization coefficient $G^{(k)}(t)$ can be replaced

by an average depolarization coefficient, $\langle G^{(k)} \rangle$, as given in Equations 51 and 53.

3. $t \approx \tau$: In this range, the time dependence of the depolarization becomes significant.

Within Regime 3, for an essentially instantaneous event that occurs at one well-defined initial time, the hyperfine depolarization can be calculated from Equation 50 or 52. Such a situation occurs, for example, in optical pumping of molecules, or photodissociation. However, for a reaction initiated at $t = 0$ and observed at a later time, $t = t'$, because individual reaction events occur with equal probability throughout the time range (assuming no depletion of reagents) and products formed at early times undergo hyperfine depolarization for a longer time than those formed at later times, we must use a cumulative hyperfine depolarization coefficient:

$$G^{(k)}_{\text{cum}}(t') = \frac{1}{t'} \int_0^{t'} G^{(k)}(t)\, dt. \qquad 55.$$

Orr-Ewing et al (131) calculated this cumulative depolarization coefficient for HCl to illustrate the effects of depolarization on aligned reagents.

In the analysis of $(1+1)$ LIF and $(1+1)$ REMPI, we must also consider the effect of hyperfine coupling to the rotational angular momentum of the intermediate state, $|J_e M_e\rangle$. The absorption of the first photon creates an excited state ensemble that is aligned or oriented and that can depolarize prior to fluorescence or absorption of an ionizing photon. Such depolarization is of no concern in the $(2+1)$ REMPI analysis because the ionization step is assumed to be saturated and thus independent of the alignment of the intermediate state.

Saturation Effects

Many researchers using LIF to study reaction dynamics or kinetics assume that the excited state population is proportional to the laser intensity. This assumption is generally valid at low laser intensities but fails as the laser power increases; the nonlinear intensity behavior that is observed is termed saturation. The high-peak intensities common with pulsed laser systems can result in partial saturation of many atomic and molecular spectral transitions. Under partial or complete saturation conditions, the dependence of the polarized LIF intensity on ground-state alignment and orientation moments deviates from the forms described previously. Altkorn & Zare (132) have used a rate-equation model to treat saturation effects in LIF using both polarized laser excitation and polarization-resolved fluorescence detection. For a cylindrically symmetric system, they show

that in moderately saturated regimes, the fluorescence intensity depends on higher moments of the angular distribution than the $A_0^{(4)}$ alignment moment, which is the highest order moment that can be determined under unsaturated conditions. This sensitivity to higher-order moments makes the polarization data difficult to interpret quantitatively. In the strongly saturated limit, only the $A_0^{(2)}$ alignment moment can be obtained. Janssen et al (133) extended the Altkorn & Zare (132) analysis to allow inversion of data within the regime of partial saturation to obtain alignment parameters in the high-J limit and applied their analysis to experimental data obtained by Engelke & Meiwes-Broer (34) on the $Ca + F_2$ and $Ca^* + HF$ reactions. Bergmann and coworkers (134) have demonstrated the application of saturated optical pumping and LIF detection to select single $|M|$ levels and to determine the population of single $|M|$ states.

Altkorn & Zare (132) consider the high-J limit of rotational polarization, and they show that for a ground-state anisotropic distribution of angular-momentum vectors described the usual Legendre-polynomial expansion given in Equation 9. The LIF intensity for a two-level system is given by

$$I = C\,(\det)\,n(J_i) \int d\Omega \frac{\alpha_{21}\beta_{12}\rho}{(2\beta_{12}\rho + A_{21})} \left(\sum_l a_{2l} P_{2l}(\cos\theta) \right)$$

$$\times \{1 - \exp[-(2\beta_{12}\rho + A_{21})\Delta t_L]\}. \quad 56.$$

In this equation, $n(J_i)$ is the total population of state $|J_i\rangle$; A_{21} is the usual Einstein coefficient for spontaneous emission; α_{21} and β_{12} are directional (differential) Einstein coefficients, which describe the interaction of directional, polarized radiation with molecules that have a specific orientation; ρ is the density of radiation directed into the solid angle $d\Omega$; and Δt_L is the duration of the (assumed rectangular) laser pulse. In the limit of no saturation, the exponential term can be replaced by the first two terms in its Taylor expansion, and a linear dependence of LIF signal on laser intensity is observed. When the absorption step is very strongly saturated, $\beta_{12}\rho\Delta t_L \gg 1$ (and $\beta_{12}\rho \gg A_{21}$) and Equation 56 reduces to

$$I = \tfrac{1}{2}C\,(\det)\,n(J_i) \int d\Omega [1 + a_2 P_2(\cos\theta)]\alpha_{21} \qquad 57.$$

(terms with Legendre polynomials of order greater than two integrate to zero). The experiment has become equivalent to performing an excited-state emission experiment because the ground state is detected independently of its alignment and the laser polarization, so only the determination of $A_0^{(2)}$ is possible. Note that polarization resolution of the fluorescence or dispersal and resolution of the fluorescence into P, Q, and

R branches becomes necessary to obtain any information about the ground-state alignment under fully saturated excitation conditions. Equation 57 is independent of the Einstein B coefficients and laser power because half the molecules in the probed state are excited, regardless of their line strengths.

Four-Wave Mixing Techniques as a Probe of Orientation and Alignment

Spectroscopic probes that make use of four-wave mixing, such as coherent anti-Stokes Raman spectroscopy (CARS) (135, 136) and degenerate four-wave mixing (DFWM) (137–141), have proved valuable for the detection of trace species in radiant, high-pressure (hostile) environments, such as flames and plasmas, and have been applied, albeit in a limited number of cases, to experimental studies of molecular dynamics (142–144). Attal-Trétout et al (145) gave analytical forms for the line strengths of CARS transitions, and their work has been extended by Aben et al (146), Berman et al (147), Kupiszewska & Whitaker (148), Bervas et al (149), and Williams et al (150), who have calculated line strengths for DFWM. These calculations demonstrate that the intensity of four-wave mixing signal and the degree of polarization of the signal beam depend strongly on the polarizations of the three input beams and the rotational transition probed. The dependence on beam polarizations is a consequence of contributions to the signal from polarization gratings that arise from coherent excitation of the M states of the probed molecules within the overlap region of the three input laser beams. Williams et al (150) discussed the DFWM response in terms of the zeroth-, first-, and second-rank spherical-tensor moments of the angular-momentum distribution induced by the DFWM process. The calculations of Williams et al (150) should be readily extended to understand the effects of an oriented or aligned sample on DFWM signal intensity. The detection of orientation and alignment by four-wave mixing is still in its infancy. We expect that this technique will prove very sensitive to angular-momentum polarization and anticipate its application to the study of species for which LIF and REMPI are not convenient probes.

EXPERIMENTAL STRATEGIES FOR MEASURING ROTATIONAL POLARIZATION FOR THE PRODUCTS OF REACTIVE COLLISIONS

To determine the spatial anisotropy of reactive scattering experimentally, we need to break the spherical symmetry commonly encountered in bulb experiments. This symmetry breaking has generally been achieved by molecular beam methods, using either crossed-beam or beam-gas con-

figurations. Recently, new techniques involving photolysis of a molecular precursor as a source of translationally aligned, hot atoms have been used. This section focuses on this approach, which was principally developed by the groups of Bersohn, Hall, Hancock, Simons, and Zare, and on the use of molecular beams.

Crossed-Beam Experiments

The products of a simple chemical reaction of the type of Equation 1 are scattered with azimuthal symmetry about the relative velocity of the reagents, $\mathbf{k}$. Thus, whenever a measurement of angular momentum distributions is desired, experiments are designed in which $\mathbf{k}$ is well defined. A crossed-beam experiment precisely defines the direction of $\mathbf{k}$ in the laboratory frame (to within the uncertainty of the spread in velocities of the two beams and their angular divergence). The relative velocity provides an axis of cylindrical symmetry about which $\mathbf{J}$-distribution measurements give the moments $\langle P_n(\hat{\mathbf{J}} \cdot \hat{\mathbf{k}}) \rangle$ directly. As discussed in subsequent sections, other experimental techniques measure the distribution of $\mathbf{J}$ about alternative laboratory-frame symmetry axes, and the frame transformation between the fundamental symmetry axis $\mathbf{k}$ and the laboratory-frame axis results in reduced sensitivity of the experiment. The crossed-beam method for the determination of product alignment has been used extensively by Herschbach and coworkers (12–15), Simons and coworkers (24–29), and Engelke & Meiwes-Broer (34); the results of these studies were described earlier.

Beam-Gas Experiments

In a beam-gas experiment, a beam of one reagent is directed into a thermal gas of the second reagent. The principal advantage of this experimental configuration over crossed beams is the substantial gain in signal that accompanies the use of a target gas. The beam axis $\mathbf{Z}$ defines an axis of cylindrical symmetry in the experiment, and for a stationary ensemble of target gas molecules, also defines the direction of the relative velocity of the reactive collisions. The target gas is generally thermal at 300 K, and the molecules of the gas move randomly with velocities that add to the beam reagent velocity to give a resultant distribution of relative velocities that differs from the stationary target-gas approximation. Zare and coworkers (22) showed that in the high-J limit, the Legendre moments of the distribution of $\mathbf{J}$ about the beam axis can be factored using the azimuthally averaged addition theorem in terms of the Legendre moments about the relative velocity according to

$$\langle P_n(\hat{\mathbf{J}} \cdot \hat{\mathbf{Z}}) \rangle = \langle P_n(\hat{\mathbf{k}} \cdot \hat{\mathbf{Z}}) \rangle \langle P_n(\hat{\mathbf{J}} \cdot \hat{\mathbf{k}}) \rangle. \qquad 58.$$

The moments $\langle P_n(\hat{\mathbf{J}} \cdot \hat{\mathbf{Z}}) \rangle$ are experimentally determined, whereas the $\langle P_n(\hat{\mathbf{J}} \cdot \hat{\mathbf{k}}) \rangle$ moments contain the desired dynamical information. The remaining term, $\langle P_n(\hat{\mathbf{k}} \cdot \hat{\mathbf{Z}}) \rangle$, is a so-called kinematic-blurring factor that describes the extent to which the relative-velocity vector and the beam axis coincide or differ as a consequence of the thermal motion of the target gas. Clearly, if the kinematic-blurring factor is small in magnitude, the laboratory-frame alignment parameters referenced to $\mathbf{Z}$ will be much smaller than the alignment parameters referenced to $\mathbf{k}$. Using Monte-Carlo methods, Prisant et al (22) calculated the magnitude of the kinematic-blurring factor with $n = 2$ for an effusive metal-atom beam impinging on a thermal gas. Johnson et al (30) extended these calculations to include supersonic and rotor-accelerated beam sources and developed two dimensionless parameters that determine the degree of the kinematic blurring. The conclusion of both groups was that the kinematic-blurring factor is generally greater than 0.8; hence, the loss of alignment information resulting from beam-gas experiments rather than crossed-beam experiments is small. The kinematic blurring is least for heavy, slow-moving targets or gases held at low temperature. Kettleborough & McKendrick (151) gave an analytical expression for the distribution function for the relative velocities of the reagents in a beam-gas experiment in which the beam is generated from an effusive source. These authors also described how to calculate the kinematic-blurring factor for $n = 2$ without the need for Monte-Carlo sampling; a numerical integration is still required, however.

The beam-gas experimental method has been applied to several reactions that result in electronically excited products that then chemiluminesce; examples were given in an earlier section. As discussed previously, the polarization of the chemiluminescence parallel and perpendicular to the beam axis can be used to determine the alignment parameters. We reiterate the principal limitation of this technique: determining quantum-state-resolved alignment parameters has proved possible in only one experimental case (23), and in that example, vibrational but not rotational state resolution was achieved.

Photoinitiated Bulb Experiments With Translationally Hot Atoms

The difficulties associated with obtaining quantum-state-resolved angular momentum polarization data from crossed-beam and beam-gas experiments have led to the development of an alternative strategy that does not rely on beams, and hence is not hindered by the very low signal levels that beam experiments give. Studies have shown that the use of photodissociation of a molecular precursor to generate one translationally hot

reagent can give vibrationally and rotationally resolved alignment information for the products of bimolecular reactions, when coupled with a laser detection method such as LIF or REMPI (39, 40, 43). The reaction scheme in these pump-and-probe experiments can be represented as

$$AX + h\nu \rightarrow A + X,$$

$$A + BC \rightarrow AB + C. \qquad\qquad 59.$$

The method for extracting AB rotational alignment relies on the A atoms being translationally hot and translationally aligned. By translationally hot, we simply mean that the A-atom speeds are substantially in excess of those of the thermal target gas BC, which commonly occurs for photolytic sources of radicals and atoms. By translationally aligned, we mean that the distribution of A velocities is anisotropic in the laboratory frame. Translational alignment is readily achieved by photodissociation using linearly polarized light (we denote the polarization vector of the photolysis light by $\mathbf{E}_{ph}$). The center-of-mass angular distribution of photofragments A resulting from the photolysis of a molecule AX using linearly polarized light is (104)

$$w(\hat{\mathbf{v}}_A, \hat{\mathbf{E}}_{ph}) = \frac{1}{4\pi}\{1 + \beta P_2(\hat{\mathbf{v}}_A \cdot \hat{\mathbf{E}}_{ph})\}, \qquad\qquad 60.$$

where β is the well-known anisotropy parameter. β takes values in the range -1 to 2, with $\beta = -1$ corresponding to a $\sin^2\theta$ distribution of $\mathbf{v}_A$ about $\mathbf{E}_{ph}$, and $\beta = +2$ corresponding to a $\cos^2\theta$ distribution of $\mathbf{v}_A$ about $\mathbf{E}_{ph}$. In the limit of A having a much higher velocity than the thermal BC, the distribution of relative velocities for the reactive collisions is identical to the distribution of A velocities given in Equation 60. However, as is true for beam-gas reactions, the velocities of the BC targets are generally not negligible, and allowance should be made for them. Green et al (39, 40) developed an analytical form for the distribution of relative velocities arising from a single speed of A in a bulb experiment of the type described here that takes into account the thermal motion of BC. These authors used numerical integration to account for the thermal motion of the AX and the spread in speeds of A from the photodissociation. Aoiz et al (152) and McKendrick and coworkers (38, 153) extended these calculations using analytical methods to account for the effect of the thermal motion of the AX photolysis precursor in addition to the thermal motion of the BC target; the latter authors obtained the compact expression for the distribution of relative velocities:

$$w(\mathbf{k}, \mathbf{E}_{ph}) \, dk \, d(\hat{\mathbf{k}} \cdot \hat{\mathbf{E}}_{ph}) = g(k)\{1 + \beta_{eff}(k)P_2(\hat{\mathbf{k}} \cdot \hat{\mathbf{E}}_{ph})\} \, dk \, d(\hat{\mathbf{k}} \cdot \hat{\mathbf{E}}_{ph}), \qquad 61.$$

where $\beta_{\text{eff}}(k)$ is an effective anisotropy parameter. This parameter has some velocity dependence:

$$\beta_{\text{eff}}(k) = \beta \frac{I_{5/2}(kv_A/\rho^2)}{I_{1/2}(kv_A/\rho^2)}, \tag{62.}$$

$$g(k) = \frac{1}{2\rho^2} \sqrt{\frac{k^3}{v_A}} \exp[-(k^2 + v_A^2)/2\rho^2] I_{1/2}(kv_A/\rho^2), \tag{63.}$$

$$\rho^2 = \frac{k_B T(m_{AX} + m_{BC})}{m_{AX} m_{BC}}, \tag{64.}$$

where k_B is Boltzmann's constant, m_{BC} is the mass of the target gas, m_{AX} is the mass of the photolysis precursor, and $I_{1/2}$ and $I_{5/2}$ are modified spherical Bessel functions (154). McKendrick and coworkers (153) then considered the consequences of Equation 61 for polarization measurements from hot-atom reactions. They examined the velocity dependence of β_{eff} for three very different mass combinations, the reactions $H + O_2$, $O(^3P) + CS$, and $O(^3P) + H_2$. For the $H + O_2$ reaction, β_{eff} is virtually independent of k and is close to its limiting value of β for all photolytically generated H-atom velocities. Consequently, speed and angular variables in Equation 61 are essentially separable. For the $O(^3P) + CS$ reaction, with oxygen atoms formed by 355-nm photolysis of NO_2 in coincidence with $NO(v = 0)$, the angular and speed terms are also approximately separable, although β_{eff} is reduced from β by 10–20%. For the reaction of $O(^3P) + H_2$, however, the light target gas has such high thermal velocities that β_{eff} is substantially reduced from β, and angular and speed terms in Equation 61 cannot be separated. The average reduction in anisotropy of the relative velocity caused by thermal motion is greater than 60%. The consequences of this reduction on polarization measurements in hot-atom reactions will become apparent from the following discussion.

The form of Equation 61, which links the laboratory frame, defined by the cylindrical-symmetry axis $\mathbf{E}_{\text{ph}}$, to the relative-velocity frame, means that the frame transformation from center of mass to the laboratory eliminates all the alignment moments except for the zeroth and second order terms. This limitation can be overcome by Doppler-resolved measurements (vide infra) or by the novel three-dimensionally resolved experiments described later. The AAA theorem permits us to write

$$\langle P_2(\hat{\mathbf{J}} \cdot \hat{\mathbf{E}}_{\text{ph}}) \rangle = \langle P_2(\hat{\mathbf{k}} \cdot \hat{\mathbf{E}}_{\text{ph}}) \rangle \langle P_2(\hat{\mathbf{J}} \cdot \hat{\mathbf{k}}) \rangle. \tag{65.}$$

The kinematic-blurring factor in this case is given by

$$\langle P_2(\hat{\mathbf{k}} \cdot \hat{\mathbf{E}}_{\text{ph}}) \rangle = \tfrac{1}{5}\beta_{\text{eff}}, \tag{66.}$$

and using the connection between Legendre moments and alignment parameters, we obtain (with vectors in parentheses denoting the reference axes for the alignment parameters)

$$A_0^{(2)}(\hat{\mathbf{E}}_{ph}) = \tfrac{1}{5}\beta_{eff}A_0^{(2)}(\hat{\mathbf{k}}).$$ 67.

Knowledge of the anisotropy parameter for the AX photodissociation is clearly necessary to make the laboratory to center-of-mass frame conversion. Equation 67 shows the most obvious drawback to this technique: The factor of $\beta_{eff}/5$ associated with the center-of-mass to laboratory-frame transformation substantially decreases the limiting ranges that the alignment can take in the laboratory frame, i.e. the best that can be hoped for in the laboratory frame is an alignment that is 40% of that in the center-of-mass frame. This limitation puts severe restrictions on the sensitivity of bulb experiments that use translationally aligned atoms to the alignment of reaction products and, as discussed above, is especially disadvantageous for systems such as the reaction of $O(^3P)+H_2$. The technique of bulb experiments that use velocity-aligned reagents, as described in this section, has been applied successfully to several reactions mentioned in a preceding section.

Reaction Product Vector Correlations From the Analysis of Doppler Profiles

Photoinitiated bulb reaction methods combined with sub-Doppler LIF detection can give information about correlations between the vectors $\mathbf{J}_{AB}$, $\mathbf{k}$, and $\mathbf{k}'$, in addition to the $A_0^{(2)}(\hat{\mathbf{k}})$ parameter. The use of Doppler-profile analysis to extract vector correlations for the products of bimolecular reactions is similar to the bipolar-moment analysis of Dixon (155), which is used widely in photodissociation studies (112). For bimolecular reactions, the bipolar-moment approach has been considered within two kinematic regimes: (a) negligible center-of-mass velocity and (b) significant center-of-mass velocity.

Within Regime a, the Doppler profiles can be used to extract correlations between the vectors $\mathbf{k}$, $\mathbf{k}'$, and $\mathbf{J}_{AB}$, including the second moment of the differential cross section (which can be written as a reactive anisotropy parameter, β_r). The fitting and analysis of Doppler profiles within this regime is similar to the procedure for photodissociation and yields analogous results in terms of bipolar moments. As shown by Hancock and coworkers (41, 58) and Brouard et al (44), Equation 9 of Dixon (155) gives the correlated distribution of reaction product velocities and angular momenta, but the frame-transformation factor of 2/5 is replaced by one of $\beta/5$, with β being the anisotropy parameter for the photodissociation

of AX (the same kinematic-blurring effects as discussed in the preceding section must be taken into account). This analysis results in a set of bipolar moments, $\beta_q^{(k)}(k_t, k_r)$, similar to those used for photodissociation studies, which are rescaled from those used in photodissociation by a factor of $\beta/2$ for the moments with $k = 2$ and are referenced to the relative-velocity vector $\mathbf{k}$ rather than the transition dipole $\boldsymbol{\mu}$. Other than these changes, when the center-of-mass velocity is negligible, the analysis of reaction-product Doppler profiles is the same as that of Dixon for photodissociation products.

When the center-of-mass velocity cannot be neglected, the Doppler-profile analysis becomes somewhat more involved, but Brouard and coworkers (44, 45, 152) showed that one can deduce vector-correlation information and differential-cross-section information that is more complete than the second moment of the scattering distribution. They developed an analysis based on velocity-dependent bipolar moments and Fourier-transform methods and advocate using composite lineshapes constructed from Doppler profiles taken at different experimental geometries. If correct linear combinations of the experimental profiles are coadded, the resultant composite profiles lose their dependence on certain bipolar moments, and the laboratory-frame speed distribution of the AB reaction product can be deduced. Back simulation of this speed distribution with trial functions can then be used to deduce features of the differential cross section. Hall and coworkers (49) developed an equivalent analysis to extract dynamical information from OH Doppler lineshapes for the product of the reaction of H with O_2. The experimental Doppler profiles are fitted to a set of basis functions that are calculated for different scattering angles and angular-momentum polarizations.

McCaffery and coworkers (97, 156–161) developed a variety of sub-Doppler and circular dichroism experiments that use optical-double-resonance methods to measure differential cross sections and vector correlations for inelastic scattering. In principle, the method could also be applied to reactions. Rather than using molecular photodissociation to prepare translationally aligned reagents, they used a particular velocity subgroup of the thermal BC molecules pumped by a narrow-bandwidth laser to an excited state and monitored the change in the excited-state velocity distribution caused by inelastic scattering. If excitation is performed in the wings of the Doppler profile for the thermal AB using circular polarization, excited state AB* forms with its velocity and rotational-angular-momentum vectors preferentially parallel; however, excitation at the center of the Doppler profile prepares $\mathbf{J}_{AB}$ preferentially perpendicular to the velocity. The sub-Doppler experiments performed with circularly polarized lasers are sensitive to four vector quantities, $\mathbf{v}_{BC}$,

$\mathbf{J}_{BC}$, $\mathbf{v}_{AB}$, and $\mathbf{J}_{AB}$ (for inelastic scattering, BC and AB are the same molecule before and after the scattering event), and McCaffrey's group applied these methods to the measurement of a four-vector correlation for the scattering of Li_2 from Xe in bulb experiments (162, 163).

VARIATION OF ORIENTATION AND ALIGNMENT WITH SCATTERING ANGLE FROM PHOTOINITIATED BULB EXPERIMENTS

Together with Shafer, Simpson, and Xu (164–166) we have recently developed a novel method that provides detailed information about the rotational anisotropy of reaction products at a quantum-state-resolved level, and this rotational anisotropy can be measured for different product scattering angles. Thus, we have demonstrated that we can measure differential cross sections that are $|J_{AB}M_{AB}\rangle$-state resolved. In this section, we first discuss the principles behind our technique and illustrate its implementation. We then show how optical-state selection of one reagent can be used to approach the goal alluded to in the title of this section, $|J_{BC}M_{BC}\rangle \rightarrow |J_{AB}M_{AB}\rangle$ specific differential cross sections.

The experimental method we use (164–166) has the following key features:

1. We use a photoinitiated reaction scheme.
2. The reagent BC and precursor AX are diluted in helium and co-expanded through a pulsed nozzle. This procedure ensures a translationally cooled system.
3. AX is photolysed to initiate reaction; the A atoms are translationally hot and "see" stationary targets BC because of the coexpansion.
4. In some experiments, we optically pump reagent BC to an excited vibrational state, with rotational state selection; otherwise, we assume that BC is in a single vibrational and rotational state because of the cooling in the expansion. Either way, we are reacting state-selected reagents.
5. After a delay of up to 200 ns after the photolysis laser pulse, we probe the reaction product AB using a laser. The key to obtaining the differential cross section and resolving the rotational anisotropy is to make a full velocity distribution measurement of the AB product with three-dimensional resolution (164). As we discuss below, a three-dimensional measurement of the velocity can, under conditions of favorable kinematics and energetics, give a direct reading of the differential cross section.

Shafer et al (164) showed that for a state-to-state reaction performed

under bulb conditions using a photolytic precursor AX to generate fast A atoms, the differential cross section can be related to the laboratory-frame velocity of the product AB via

$$f(\mathbf{v}_{AB}) = \frac{1}{2v_{AB}uu_{AB}} \frac{1}{\sigma} \frac{d\sigma}{d\Omega} \{1 + \beta P_2(\hat{\mathbf{v}}_{AB} \cdot \hat{\mathbf{u}})P_2(\hat{\mathbf{v}}_{AB} \cdot \hat{\mathbf{E}}_{ph})\}$$

$$v_{min} < v_{AB} < v_{max}, \quad 68.$$

$$f(\mathbf{v}_{AB}) = 0 \quad v_{AB} < v_{min} \quad \text{or} \quad v_{AB} > v_{max}. \quad 69.$$

Figure 6 shows a simplified Newton diagram for the reactive system that treats the velocity of BC as negligible. The relative velocity of the reagents lies parallel to the center-of-mass velocity. All labels for the vector quantities have been defined in Table 1. $(1/\sigma)(d\sigma/d\Omega)$ is the normalized differential cross section, β is the anisotropy parameter for the AX photodissociation, and v_{min} and v_{max} are defined by

$$v_{min} = |u - u_{AB}| \quad\quad 70.$$

and

$$v_{max} = |u + u_{AB}|. \quad\quad 71.$$

Two experimental strategies for making the three-dimensionally resolved AB velocity measurement have been proposed, both of which
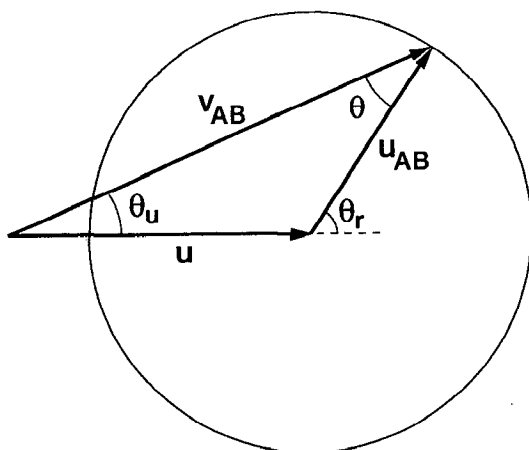

Figure 6 Simple Newton diagram for photoinitiated-bulb reactions with the photolytic precursor, XA, and the reagent BC cooled in a supersonic expansion. θ_r is the center-of-mass scattering angle, **u** is the velocity of the center of mass, $\mathbf{u}_{AB}$ and $\mathbf{v}_{AB}$ are the velocities of the product AB in the center-of-mass and laboratory frames respectively. The relative velocity of the reagents lies parallel to **u**.

make use of multiphoton ionization techniques to detect the AB product. In both cases, the reagents are prepared as in Steps 1–5 above. The detection method of Shafer et al (165) uses a three-photon ionization scheme, which we refer to as $(1 + 1' + 1'')$ REMPI, and sub-Doppler bandwidth lasers and time-of-flight mass spectrometry (TOF/MS) of the ions to probe the products in a velocity-selective fashion. The use of velocity resolution via time-of-flight mass spectrometry is also a key feature of the method used by Simpson et al (166).

Mons & Dimicoli (167, 168) and others discussed the use of REMPI coupled with time-of-flight (TOF) spectroscopy to measure velocity distributions of photofragments. Ions are formed by $(1 + 1)$ or $(2 + 1)$ REMPI of photofragments in the extraction region of a linear time-of-flight mass spectrometer. The TOF profile for any one mass corresponds to a one-dimensional projection of the photofragment velocity distribution onto the TOF axis. The precise details of the inversion from time of flight to velocity depend on the voltages used in the acceleration regions of the spectrometer and on whether the voltages are pulsed or continuous. The ideas developed for photodissociation experiments are also applicable to bimolecular reactions, and Simpson et al (166) demonstrated the use of TOF/MS to obtain state-to-state resolved differential cross sections for the reaction

$$Cl(^2P_{3/2}) + CH_4(v_3 = 1, J = 1) \rightarrow HCl(v' = 1, J') + CH_3, \qquad 72.$$

with $J' = 0, 1, 2,$ and 3.

Shafer et al (165) used the velocity sensitivity of TOF measurements to obtain the **Z** axis velocity component of reaction products, having selected the **X**- and **Y**-axis components to be zero by their Doppler technique. Simpson et al (WR Simpson, AJ Orr-Ewing & RN Zare, unpublished results) have modified the traditional TOF method to give three-dimensional velocity resolution in a different manner, dubbed core-extraction. As the ion cloud, which is formed as a near-point source by the probe laser in a REMPI process, flies down the TOF tube, it expands outward because many of the ions have components of velocity carried over from the reactive event that are perpendicular to the **Z** axis. Simpson et al (WR Simpson, AJ Orr-Ewing & RN Zare, unpublished results) selected only those ions moving parallel or antiparallel (to within the instrumental resolution) to the TOF axis by the use of a baffle placed in the TOF tube that passes only those ions with little or no velocity component away from the TOF axis.

The experiments define an axis in the laboratory, which we denote by **Z**, selectively detect product molecules in a particular $|v_{AB}J_{AB}\rangle$ quantum state, and resolve the AB velocity along **Z**. The velocity resolution differs

from the Doppler profile method (41, 43–45, 49, 58, 152) or the ion-imaging technique (119, 121, 169, 170) because the velocity resolution along $\mathbf{Z}$ is not a projection of a three-dimensional distribution onto a line, nor is it a two-dimensional projection onto a plane as is used in ion imaging. The measurement of $\mathbf{v}_{AB}$ is a three-dimensionally resolved core through the velocity distribution. Thus we take the $\mathbf{Z}$-axis component of $f(\mathbf{v}_{AB})$, and the time-of-flight profiles that are recorded are a direct mapping of the differential cross section for the reaction. We can assign each point on the time-of-flight profile to a particular scattering angle in the center-of-mass frame (to within the resolution of the instrument), and thus, a study of the polarization dependence of each point on the profile gives the rotational angular momentum anisotropy of the AB product as a function of the scattering angle.

By changing the polarization of the probe laser(s) with respect to the $\mathbf{Z}$ axis, we have a method that is sensitive to the alignment moments of the AB referenced to the $\mathbf{Z}$ axis, i.e. we measure the distribution of $\mathbf{J}_{AB}$ about $\mathbf{v}_{AB}$. We can convert this laboratory-frame alignment, or orientation, to the frame of the relative velocities of the reagents, as is typically done for bimolecular reactions, but there is an equally simple frame transformation we can make to relate the scattering-angle resolved alignment and orientation parameters to the velocity of the product AB in the center-of-mass frame, $\mathbf{u}_{AB}$.

The angles and geometries needed are defined in Figure 7. Note that several different center-of-mass velocities, $\mathbf{u}$ (and relative velocities, $\mathbf{k}$), can result in the measured laboratory velocity $\mathbf{v}_{AB}$ for a single speed u_{AB}, and the possible values of $\mathbf{u}$ lie on a cone as shown in Figure 7. Thus we must average over the azimuthal angle about $\mathbf{v}_{AB}$, and this averaging is complicated by the fact that unless $\mathbf{E}_{ph}$ lies parallel to $\mathbf{v}_{AB}$, the azimuthal angle is not uniformly distributed. Using both the real parameters, $A_{\pm q}^{(k)}(J)$, defined in Equation 26, and the complex parameters, $\mathscr{A}_{\pm q}^{(k)}(J)$, defined in Equation 27, we derived expressions for the orientation and alignment parameters in the frame of $\mathbf{u}_{AB}$. The frame transformation of the real alignment parameters requires the use of real rotation matrices and, thus, is a more complicated procedure than the transformation of $\mathscr{A}_{\pm q}^{(k)}(J)$. We know the angles between the $\mathbf{v}_{AB}$ and $\mathbf{u}_{AB}$ frames (see Figure 6) and can therefore interrelate the alignment parameters. We obtain the relationships

$$\mathscr{A}_q^{(k)}(\mathbf{v}_{AB}) = H_q(0_r, \Theta, 0) \sum_{q'=-k}^{k} d_{qq'}^{(k)}(\theta)\mathscr{A}_{q'}^{(k)}(\mathbf{u}_{AB}), \qquad 73.$$

$$A_q^{(k)}(\mathbf{v}_{AB}) = H_q(\theta_r, \Theta, \theta) \sum_{q'=-k}^{k} d_{qq'}^{(k)}(\theta)A_{q'}^{(k)}(\mathbf{u}_{AB}), \qquad 74.$$
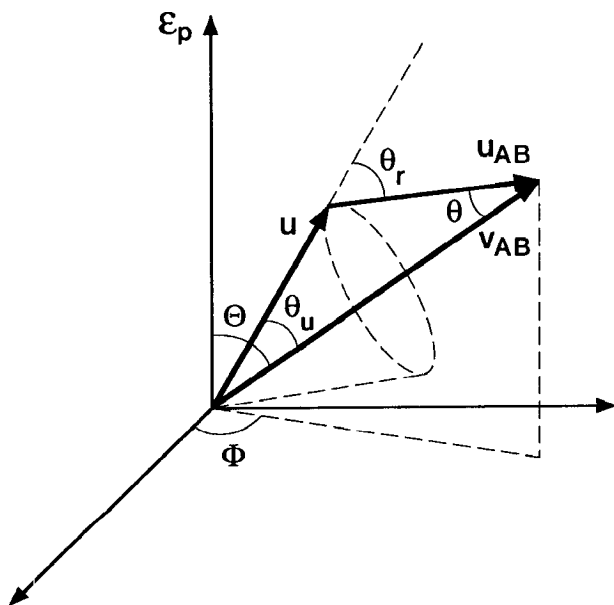
Figure 7 Geometries and angles for analysis of the alignment and orientation of reaction products from photoinitiated bulb reactions.
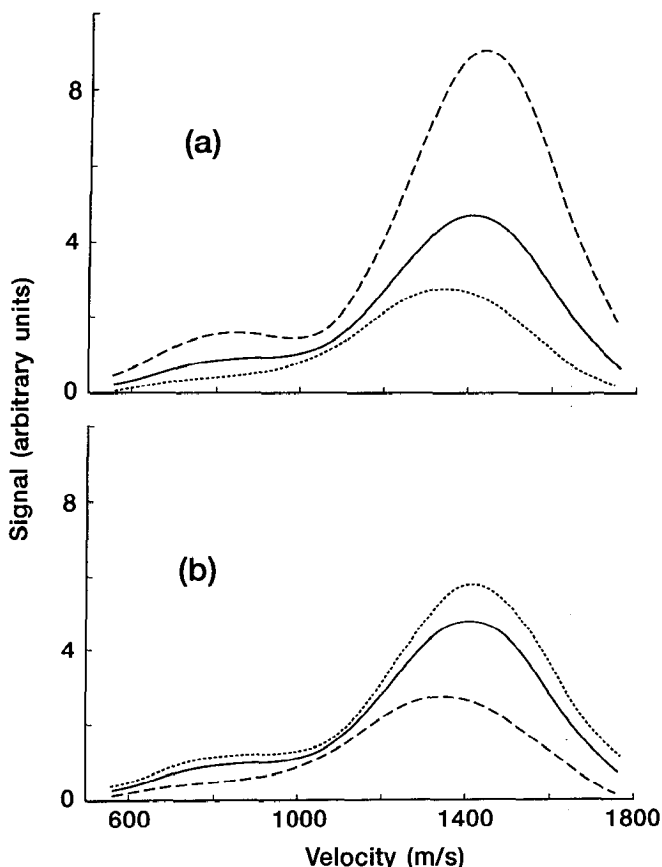
with

$$
H_q(\theta_r, \Theta, \theta) = \begin{cases} 1 & q = 0 \\ \dfrac{\beta P_2(\cos\theta_r)\, d_{q0}^{(2)}(\theta)\, d_{q0}^{(2)}(\Theta)}{1 + \beta P_2(\cos\theta_r)\, P_2(\cos\Theta)\, P_2(\cos\theta)} & q \neq 0 \end{cases}
\qquad 75.
$$

We see from Equations 73–75 that the component, q, is restricted to values of $q \leqslant 2$. If we consider a simple example of alignment parameters with $k = 2$, a measurement of the five parameters $\mathscr{A}_q^{(k)}(\mathbf{v}_{AB})$ with $q = 0$, ± 1, and ± 2 allows inversion of Equation 73 or 74 to give the $\mathscr{A}_{q'}^{(k)}(\mathbf{u}_{AB})$ with $k = 2$. We can also calculate the relationship between alignment parameters in the frames of $\mathbf{v}_{AB}$ and $\mathbf{u}$. We obtain very similar results to Equations 73–75 but with $H_q(\theta_r, \Theta, \theta_u)$ replaced by $h_q(\theta_r, \Theta, \theta_u)$, where

$$
h_q(\theta_r, \Theta, \theta) = \begin{cases} 1 & q = 0 \\ \dfrac{\beta d_{q0}^{(2)}(\theta_u)\, d_{q0}^{(2)}(\Theta)}{1 + \beta P_2(\cos\theta_u) P_2(\cos\theta)} & q \neq 0 \end{cases}
\qquad 76.
$$

In Figure 8 we simulated differential cross section data using the core-extraction method for highly aligned $HCl(v' = 1, J' = 1)$ obtained from

Figure 8 Simulated core-extraction data for the HCl($v' = 1, J' = 1$) product of the reaction of Cl($^2P_{3/2}$) with CH$_4$($v_3 = 1$) using the measured differential cross section, and including possible alignment effects. The simulation is for HCl detection via the F($^1\Delta$) state on the R(1) transition, with the probe laser polarized parallel and perpendicular to the photolysis laser. (*a*) $A_0^{(2)} = +2$, and (*b*) $A_0^{(2)} = -1$, with the long dashed line denoting the horizontally polarized probe laser, the short dashed line denoting the vertically polarized probe laser, and the solid line denoting the signal for no alignment.

the reaction of Cl($^2P_{3/2}$) with CH$_4$($v_3 = 1, J = 1$). The simulations clearly demonstrate that the method discussed here is extremely sensitive to product rotational alignment and orientation. The method is, on the whole, much more sensitive than the velocity-aligned experiments described earlier because the blurring caused by the center-of-mass frame to laboratory-frame transformation is significantly reduced. The principal disadvantage is that this sensitivity is at the expense of a loss of signal compared with

collection of all the ions formed; however, compared with collection of LIF into a small solid angle, the signal loss is not substantial. The alignment parameters can be expressed in either the $\mathbf{u}_{AB}$ or $\mathbf{u}$ ($\parallel \mathbf{k}$) frames, and thus we arrive at the same information that is contained within a bipolar moment description of the rotational angular momentum distribution of AB because we can correlate $\mathbf{u}$ ($\mathbf{k}$), $\mathbf{u}_{AB}$, and $\mathbf{J}_{AB}$. The orientation and alignment parameters are, however, scattering-angle resolved.

If, as in the experiments of Simpson et al (166), a polarized excitation beam is used in the state selection of the BC reagent, then the state-selected BC is rotationally aligned in the frame of the polarization of the excitation laser. This alignment is retained to some extent in the collision frame, i.e. with respect to the relative velocities of the reagents. We can write down a density-matrix representation of the M_{BC} population distribution in the frame of reference of the excitation polarization, and this density matrix can be transformed into the frame of the relative velocity. Thus we have a density matrix description of the M_{BC} populations and coherences in the frame of $\mathbf{k}$, and we measure the alignment parameters of the AB reaction product, which we can transform to the frame of $\mathbf{k}$ or $\mathbf{u}_{AB}$. We can determine this alignment for different center-of-mass scattering angles. We note that for $R(0)$ excitation and for the polarization of the excitation beam parallel to the velocity-resolution axis, $\mathbf{v}_{AB}$, a single state, $|J_e = 1, M_e = 0)$, is prepared in the collision frame for the formation of forward- or backward-scattered products.

The density-matrix elements in the collision frame for a photoinitiated bulb experiment in which a one-dimensional velocity projection (Doppler or TOF profile) of the product velocities is made has only diagonal matrix elements because of cylindrical symmetry about the electric vector of the photolysis laser (171). If the density-matrix elements are evaluated for a specific excitation transition or are recast in terms of alignment and orientation parameters, the effect of averaging over the distribution of $\mathbf{u}$ is found to be much greater than for the experiments in which only one $\mathbf{v}_{AB}$ is resolved.

CONCLUSIONS

Developments in experimental reaction dynamics have reached the stage where spatial distributions of angular momentum vectors and velocity distributions can be probed at a state-specific level. We have discussed methods for quantifying the correlations between velocity and angular momentum vectors and shown how these vector correlations are described in terms of symmetrized operator moments termed orientation and alignment parameters. The key to studying state specifically the correlations of

J is the use of optical probes because the multipolar nature of polarized light, be it linearly, circularly, or elliptically polarized, is naturally sensitive to anisotropic distributions of **J**. The analytical techniques necessary to extract orientation and alignment parameters from spectral intensity information are firmly established in the literature. The more photons used in the optical detection method, the higher the moments of the angular momentum distribution that can be measured. We anticipate that four-wave-mixing methods will be applied to the probing of anisotropic angular momentum distributions, adding another valuable optical technique to the more commonly used LIF and REMPI methods.

The number of reactions for which product alignment has been probed has increased steadily over the past few years, and for photolytically induced reactions studied under bulb conditions, the dependence of the product alignment on rotational quantum number can be investigated. Interpretation of the experimental data has yielded new insights into elementary reaction mechanisms. No experiments have, to our knowledge, probed the orientation of reaction products, and reaction product orientation remains a topic that warrants detailed investigation.

We have demonstrated that the dependence of product orientation and alignment on the center-of-mass scattering angle of the products can be deduced from a measurement of the full product velocity distribution (in three dimensions). Optical state preparation of reagents can be used to select a distribution of M states of the reagents that mostly keeps its anisotropy on transformation to the collision frame, even for experiments conducted under bulk conditions. These and other experimental developments involving optical-detection methods demonstrate that bulb experiments, especially those in a cooled jet, can provide dynamic information that has not been forthcoming from crossed-beam and beam-gas experiments. We expect orientation and alignment measurements that are differential in angle to be made soon. The prospect of $|J, M\rangle \to |J', M'\rangle$-resolved differential cross sections promises to provide studies of chemical reaction dynamics with an unprecedented degree of detail.

Literature Cited

1. Child MS. 1974. *Molecular Collision Theory*. London: Academic
2. Bernstein RB. 1982. *Chemical Dynamics via Molecular Beam and Laser Techniques*. Oxford: Clarendon
3. Bernstein RB, Herschbach DR, Levine RD. 1987. *J. Phys. Chem.* 91: 5365–77
4. Simons JP. 1987. *J. Phys. Chem.* 91: 5378–87
5. Levine RD, Bernstein RB. 1988. *J. Phys. Chem.* 92: 6954–58
6. Levine RD. 1990. *J. Phys. Chem.* 94: 8872–80
7. Houston PL. 1987. *J. Phys. Chem.* 91: 5388–97
8. *J. Phys. Chem.* 1987. 91: 5365–5515
9. *J. Chem. Soc. Faraday Trans.* 1989. 85: 925–1376
10. *J. Chem. Soc. Faraday Trans.* 1993. 89: 1401–1592
11. Herschbach DR. 1987. *Faraday Discuss. Chem. Soc.* 84: 465–78
12. Maltz C, Weinstein ND, Herschbach DR. 1972. *Mol. Phys.* 24: 133–50
13. Hsu DSY, Herschbach DR. 1973. *Faraday Discuss. Chem. Soc.* 55: 116–19
14. Hsu DSY, McClelland GM, Herschbach DR. 1974. *J. Chem. Phys.* 61: 4927–28
15. Hsu DSY, Weinstein ND, Herschbach DR. 1975. *Mol. Phys.* 29: 257–78
16. Freund SM, Fisk GA, Herschbach DR, Klemperer W. 1971. *J. Chem. Phys.* 54: 2510–18
17. Mariella RP, Herschbach DR, Klemperer W. 1974. *J. Chem. Phys.* 61: 4575–81
18. Vaccaro PH, Tsekouras AA, Zhao D, Leach CA, Zare RN. 1992. *J. Chem. Phys.* 96: 2786–98
19. Noda C, Zare RN. 1987. *J. Chem. Phys.* 86: 3968–77
20. Hartree WS, Simons JP, González-Ureña A. 1990. *J. Chem. Soc. Faraday Trans.* 86: 17–20
21. Jonah CD, Zare RN, Ottinger C. 1972. *J. Chem. Phys.* 56: 263–74
22. Prisant MG, Rettner CT, Zare RN. 1981. *J. Chem. Phys.* 75: 2222–30
23. Prisant MG, Rettner CT, Zare RN. 1982. *Chem. Phys. Lett.* 88: 271–74
24. Rettner CT, Simons JP. 1978. *Chem. Phys. Lett.* 59: 178–81
25. Rettner CT, Simons JP. 1979. *Faraday Discuss. Chem. Soc.* 67: 329–42
26. Hennessy RJ, Simons JP. 1980. *Chem. Phys. Lett.* 75: 43–46
27. Hennessy RJ, Ono Y, Simons JP. 1980. *Chem. Phys. Lett.* 75: 47–51
28. Hennessy RJ, Simons JP. 1981. *Mol. Phys.* 44: 1027–34
29. Hennessy RJ, Ono Y, Simons JP. 1981. *Mol. Phys.* 43: 181–92
30. Johnson K, Pease R, Simons JP. 1984. *Mol. Phys.* 52: 955–68
31. Johnson K, Pease R, Simons JP, Smith PA, Kvaran A. 1986. *J. Chem. Soc. Faraday Trans.* 82: 1281–95
32. Tyndall GW, de Vries MS, Cobb CL, Martin RM. 1987. *J. Chem. Phys.* 87: 5830–39
33. Tyndall GW, de Vries MS, Cobb CL, Martin RM. 1992. *Chem. Phys. Lett.* 195: 279–85
34. Engelke F, Meiwes-Broer KH. 1984. *Chem. Phys. Lett.* 108: 132–37
35. Garay M, Menéndez M, Verdasco E, Castaño J, González-Ureña A. 1993. *J. Phys. Chem.* 97: 5836–38
36. Menéndez M, Garay M, Verdasco E, González-Ureña A. 1993. *J. Chem. Soc. Faraday Trans.* 89: 1493–99
37. Li R-J, Han K-L, Li F-E, Lu R-C, He G-Z, Lou N-Q. 1994. *Chem. Phys. Lett.* In press
38. van der Zande W, Zhang R, McKendrick KG, Zare RN, Valentini JJ. 1991. *J. Phys. Chem.* 95: 8205–7
39. Green F, Hancock G, Orr-Ewing AJ. 1991. *Faraday Discuss. Chem. Soc.* 91: 79–90
40. Green F, Hancock G, Orr-Ewing AJ, Brouard M, Duxon SP, et al. 1991. *Chem. Phys. Lett.* 182: 568–74
41. Costen ML, Hancock G, Orr-Ewing AJ, Summerfield D. 1994. *J. Chem. Phys.* 100: 2754–64
42. Brouard M, Duxon SP, Enriquez PA, Sayos R, Simons JP. 1991. *Laser Chem.* 11: 265–72
43. Brouard M, Duxon SP, Enriquez PA, Sayos R, Simons JP. 1991. *J. Phys. Chem.* 95: 8169–74
44. Brouard M, Duxon SP, Enriquez PA, Simons JP. 1992. *J. Chem. Phys.* 97: 7414–22
45. Brouard M, Duxon S, Enriquez PA, Simons JP. 1993. *J. Chem. Soc. Faraday Trans.* 89: 1435–42
46. Ben-Nun M, Brouard M, Simons JP, Levine RD. 1993. *Chem. Phys. Lett.* 210: 423–31
47. Sauder DG, Stephenson JC, King DS, Casassa MP. 1992. *J. Chem. Phys.* 97: 952–63
48. Kleinermanns K, Linnebach E. 1986. *Appl. Phys. B* 36: 203–6
49. Kim HL, Wickramaaratchi MA, Zheng X, Hall GE. 1994. *J. Chem. Phys.* In press

50. Alexander MH, Orlikowski R. 1984. *J. Chem. Phys.* 80: 1506–16
51. Dagdigian PJ, Alexander MH, Liu K. 1989. *J. Chem. Phys.* 91: 839–48
52. Alexander MH, Dagdigian PJ. 1984. *J. Chem. Phys.* 80: 4325–32
53. Alexander MH, Andresen P, Bacis R, Bersohn R, Comes FJ, et al. 1988. *J. Chem. Phys.* 89: 1749–53
54. Mariella RP, Luntz AC. 1977. *J. Chem. Phys.* 67: 5388–89
55. Mariella RP, Lantzch B, Maxson VT, Luntz AC. 1978. *J. Chem. Phys.* 69: 5411–18
56. Murphy EJ, Brophy JH, Arnold GS, Dimpfl WF, Kinsey JL. 1978. *J. Chem. Phys.* 74: 324–30
57. Andresen P, Luntz AC. 1980. *J. Chem. Phys.* 72: 5842–50
58. Orr-Ewing AJ. 1991. *Laser studies of reaction dynamics.* D. Phil. thesis. Oxford Univ.
59. Bronikowski MJ, Zare RN. 1990. *Chem. Phys. Lett.* 166: 5–10
60. Hijazi NH, Polanyi JC. 1975. *J. Chem. Phys.* 63: 2249–50
61. Hijazi NH, Polanyi JC. 1975. *Chem. Phys.* 11: 1–16
62. Schatz GC, Kuppermann A. 1976. *J. Chem. Phys.* 65: 4668–92
63. Blais NC, Truhlar DG. 1977. *J. Chem. Phys.* 67: 1540–46
64. Alvariño JM, Laganà A. 1991. *J. Chem. Phys.* 95: 998–1005
65. Alvariño JM, Laganà A. 1992. *J. Phys. Chem.* 96: 3587–90
66. Alexander MH, Dagdigian PJ, DePristo AE. 1977. *J. Chem. Phys.* 66: 59–66
67. Alexander MH, Dagdigian PJ. 1977. *J. Chem. Phys.* 66: 4126–32
68. Alexander MH, Davis SL. 1983. *J. Chem. Phys.* 79: 227–38
69. Orlikowski T, Alexander MH. 1984. *J. Chem. Phys.* 80: 4133–36
70. Khare V, Kouri DJ, Hoffman DK. 1981. *J. Chem. Phys.* 74: 2275–86
71. Khare V, Kouri DJ, Hoffman DK. 1981. *J. Chem. Phys.* 74: 2656–57
72. Khare V, Kouri DJ, Hoffman DK. 1982. *J. Chem. Phys.* 76: 4493–501
73. Prisant MG, Rettner CT, Zare RN. 1984. *J. Chem. Phys.* 81: 2699–712
74. McClelland GM, Herschbach DR. 1987. *J. Phys. Chem.* 91: 5509–15
75. Case DA, Herschbach DR. 1975. *Mol. Phys.* 30: 1537–64
76. Case DA, Herschbach DR. 1976. *J. Chem. Phys.* 64: 4212–22
77. Barnwell JD, Loeser JG, Herschbach DR. 1983. *J. Phys. Chem.* 87: 2781–86
78. Case DA, Herschbach DR. 1978. *J. Chem. Phys.* 69: 150–58
79. Case DA, McClelland GM, Herschbach DR. 1978. *Mol. Phys.* 35: 541–73
80. Fano U, Macek JH. 1973. *Rev. Mod. Phys.* 45: 553–73
81. Greene CH, Zare RN. 1982. *Annu. Rev. Phys. Chem.* 33: 119–50
82. Zare RN. 1988. *Angular Momentum. Understanding Spatial Aspects in Chemistry and Physics.* New York: Wiley
83. Hasselbrink E, Waldeck JR, Zare RN. 1989. *Chem. Phys.* 126: 191–200
84. Black JF, Waldeck JR, Zare RN. 1990. *J. Chem. Phys.* 92: 3519–38
85. Sitz GO, Kummel AC, Zare RN, Tully JC. 1988. *J. Chem. Phys.* 89: 2572–82
86. Varshalovich DA, Moskalev AN, Khersonskii VK. 1989. *Quantum Theory of Angular Momentum.* Singapore: World Scientific
87. Blum K. 1981. *Density Matrix Theory and Applications.* New York: Plenum
88. Fano U. 1957. *Rev. Mod. Phys.* 29: 74–93
89. Kummel AC, Sitz GO, Zare RN. 1986. *J. Chem. Phys.* 85: 6874–97
90. Kummel AC, Sitz GO, Zare RN. 1988. *J. Chem. Phys.* 88: 7357–68
91. Kummel AC, Sitz GO, Zare RN. 1988. *J. Chem. Phys.* 88: 6707–32
92. Hertel IV, Stoll W. 1978. *Adv. At. Mol. Phys.* 13: 113–228
93. Greene CH, Zare RN. 1983. *J. Chem. Phys.* 78: 6741–53
94. Jacobs DC, Zare RN. 1986. *J. Chem. Phys.* 85: 5457–68
95. Jacobs DC, Madix RJ, Zare RN. 1986. *J. Chem. Phys.* 85: 5469–79
96. Docker MP. 1988. *Chem. Phys.* 125: 185–210
97. Rowe MD, McCaffery AJ. 1979. *Chem. Phys.* 43: 35–54
98. Bain AJ, McCaffery AJ, Procter MJ, Whitaker BJ. 1984. *Chem. Phys. Lett.* 110: 663–65
99. Bain AJ, McCaffery AJ. 1984. *Chem. Phys. Lett.* 105: 477–79
100. Bain AJ, McCaffery AJ. 1984. *J. Chem. Phys.* 80: 5883–92
101. Bain AJ, McCaffery AJ. 1985. *J. Chem. Phys.* 83: 2627–31
102. Bain AJ, McCaffery AJ. 1985. *J. Chem. Phys.* 83: 2632–40
103. Bain AJ, McCaffery AJ. 1985. *J. Chem. Phys.* 83: 2641–45
104. Zare RN. 1972. *Mol. Photochem.* 4: 1–37
105. Bergmann K. 1988. In *Atomic and Molecular Beam Methods,* ed. G Scoles, 1: 293–344. New York: Oxford Univ. Press
106. Taatjes CA, Stolte S. 1993. *J. Chem. Soc. Faraday Trans.* 89: 1551–65

107. Hefter U, Bergmann K. 1988. See Ref. 105, pp. 193–253
108. Waldeck JR, Kummel AC, Sitz GO, Zare RN. 1989. *J. Chem. Phys.* 90: 4112–14
109. Chen K, Yeung ES. 1979. *J. Chem. Phys.* 70: 1312–19
110. Dubs M, Bruhlmann U, Huber JR. 1986. *J. Chem. Phys.* 84: 3106–19
111. Docker MP. 1989. *Chem. Phys.* 135: 405–21
112. Hall GE, Houston PL. 1989. *Annu. Rev. Phys. Chem.* 40: 375–405
113. Naher U, Bracker A, Chen XR, Jakob P, Wanner J. 1991. *J. Phys. Chem.* 95: 8376–79
114. Sitz GO, Kummel AC, Zare RN. 1987. *J. Chem. Phys.* 87: 3247–49
115. Sitz GO, Kummel AC, Zare RN. 1988. *J. Chem. Phys.* 89: 2558–71
116. Sitz GO, Farrow RL. 1990. In *Proc. 12th Combustion Res. Conf.*, Off. Basic Energy Sci., US Dep. Energy, Tahoe City, Calif.
117. Hanisco TF, Yan C, Kummel AC. 1992. *J. Phys. Chem.* 96: 2982–93
118. Powis I, Black JF. 1989. *J. Phys. Chem.* 93: 2461–70
119. Janssen MHM, Parker DH, Sitz GO, Stolte S, Chandler DW. 1991. *J. Phys. Chem.* 95: 8007–13
120. Ogorzalek-Loo R, Haerri HP, Hall GE, Houston PL. 1989. *J. Chem. Phys.* 90: 4222–36
121. Suits AG, Miller RL, Bontuyan LS, Houston PL. 1993. *J. Chem. Soc. Faraday Trans.* 89: 1443–47
122. Jacobs DC, Kolasinski KW, Madix RJ, Zare RN. 1987. *J. Chem. Phys.* 87: 5038–39
123. Jacobs DC, Kolasinski KW, Madix RJ, Zare RN. 1989. *J. Chem. Soc. Faraday Trans.* 85: 1325–35
124. Jacobs DC, Kolasinski KW, Shane SF, Zare RN. 1989. *J. Chem. Phys.* 91: 3182–95
125. Jacobs DC, Zare RN. 1989. *J. Chem. Phys.* 91: 3196–207
126. Madden PA. 1975. *Chem. Phys. Lett.* 35: 521–24
127. Altkorn R, Zare RN, Greene CH. 1985. *Mol. Phys.* 55: 1–9
128. Yan C, Kummel AC. 1993. *J. Chem. Phys.* 98: 6869–82
129. Reid KL. 1993. *Chem. Phys. Lett.* 215: 25–30
130. Altkorn R. 1984. *Studies of molecular rotation in elementary reactions utilizing laser techniques.* PhD thesis. Stanford Univ.
131. Orr-Ewing AJ, Simpson WR, Rakitzis TP, Zare RN. 1994. *Isr. J. Chem.* 34: 95–102
132. Altkorn R, Zare RN. 1984. *Annu. Rev. Phys. Chem.* 35: 265–89
133. Janssen MHM, Parker DH, Stolte S. 1987. *Chem. Phys.* 113: 357–82
134. Hefter U, Ziegler G, Mattheus A, Fischer A, Bergmann K. 1986. *J. Chem. Phys.* 85: 286–302
135. Eckbreth AC. 1988. *Laser Diagnostics for Combustion Temperature Species.* Cambridge, MA: Abacus
136. Valentini JJ. 1985. In *Spectrometric Techniques*, ed. GA Vanasse, pp. 1–61. New York: Academic
137. Abrams RL, Lam JF, Lind RC, Steel DG, Liao PF. 1983. In *Optical Phase Conjugation*, ed. RA Fisher, pp. 211–84. New York: Academic
138. Ewart P, O'Leary SV. 1986. *Opt. Lett.* 11: 279–81
139. Farrow RL, Rakestraw DJ. 1992. *Science* 257: 1894–900
140. Williams S, Green DS, Sethuraman S, Zare RN. 1992. *J. Am. Chem. Soc.* 114: 9122–30
141. Green DS, Owano TG, Williams S, Goodwin D, Zare RN, Kruger CH. 1993. *Science* 259: 1726–29
142. Valentini JJ, Gerrity DP, Phillips DL, Nieh J-C, Tabor KD. 1987. *J. Chem. Phys.* 86: 6745–56
143. Aker PM, Valentini JJ. 1993. *Int. Rev. Phys. Chem.* 12: 363–90
144. Zhang Q, Kandel SA, Wasserman AW, Vaccaro PH. 1992. *J. Chem. Phys.* 96: 1640–43
145. Attal-Trétout B, Monot P, Müller-Dethlefs K. 1991. *Mol. Phys.* 73: 1257–93
146. Aben I, Ubachs W, van der Zwan G, Hogervorst W. 1993. *Chem. Phys.* 169: 113–28
147. Berman PR, Steel DG, Khitrova G, Liu J. 1988. *Phys. Rev. A* 38: 252–62
148. Kupiszewska D, Whitaker BJ. 1993. *J. Chem. Soc. Faraday Trans.* 89: 2951–56
149. Bervas H, Le Boiteux S, Labrunie L, Attal-Trétout B. 1993. *Mol. Phys.* 79: 911–41
150. Williams S, Zare RN, Rahn LA. 1994. *J. Chem. Phys.* In press
151. Kettleborough JA, McKendrick KG. 1991. *J. Phys. Chem.* 95: 8255–63
152. Aoiz FJ, Brouard M, Enriquez P, Sayos R. 1993. *J. Chem. Soc. Faraday Trans.* 89: 1427–34
153. Gilbert EP, Maitland G, Watson A, McKendrick KG. 1993. *J. Chem. Soc. Faraday Trans.* 89: 1527–31
154. Abramowitz M, Stegun IA. 1972. *Handbook of Mathematical Functions.* New York: Dover

155. Dixon RN. 1986. *J. Chem. Phys.* 85: 1866–79
156. McCaffery AJ, Procter MJ, Whitaker BJ. 1986. *Annu. Rev. Phys. Chem.* 37: 223–44
157. McCaffery AJ. 1987. *J. Phys. Chem.* 91: 5451–55
158. McCaffery AJ, Reid KL, Whitaker BJ. 1988. *Phys. Rev. Lett.* 61: 2085–87
159. Fell CP, McCaffery AJ, Reid KL, Ticktin A. 1991. *J. Chem. Phys.* 95: 4948–57
160. Reid KL, McCaffery AJ. 1991. *J. Chem. Phys.* 95: 4958–65
161. Reid KL, McCaffery AJ. 1992. *J. Chem. Phys.* 96: 5789–96
162. Collins TLD, McCaffery AJ, Wynn MJ. 1991. *Faraday Discuss. Chem. Soc.* 91: 91–96
163. Collins TLD, McCaffery AJ, Wynn MJ. 1991. *Phys. Rev. Lett.* 66: 137–40
164. Shafer NE, Orr-Ewing AJ, Simpson WR, Xu H, Zare RN. 1993. *Chem. Phys. Lett.* 212: 155–62
165. Shafer NE, Xu H, Tuckett RP, Springer M, Zare RN. 1994. *J. Phys. Chem.* 98: 3369–78
166. Simpson WR, Orr-Ewing AJ, Zare RN. 1993. *Chem. Phys. Lett.* 212: 163–71
167. Mons M, Dimicoli I. 1986. *Chem. Phys. Lett.* 131: 298–302
168. Mons M, Dimicoli I. 1989. *J. Chem. Phys.* 90: 4037–47
169. Chandler DW, Houston PL. 1987. *J. Chem. Phys.* 87: 1445–47
170. Chandler DW, Thoman JW, Sitz GO, Janssen MHM, Stolte S, Parker DH. 1989. *J. Chem. Soc. Faraday Trans.* 85: 1305–9
171. Orr-Ewing AJ, Zare RN. 1994. In *Chemical Dynamics and Kinetics of Small Free Radicals*, ed. K Liu, A Wagner. Singapore: World Scientific. In press
172. Jalink H, Parker DH, Stolte S. 1986. *J. Chem. Phys.* 85: 5372–73